



1 **Aerosol chemistry, transport and climatic implications during extreme biomass**  
2 **burning emissions over Indo-Gangetic Plain**

3 **Nandita Singh<sup>1</sup>, Tirthankar Banerjee<sup>1,2</sup>, Made P. Raju<sup>3</sup>, Karine Deboudt<sup>4</sup>, Meytar Sorek-Hamer<sup>5</sup>,**  
4 **Ram S. Singh<sup>2,6</sup> and Rajesh K. Mall<sup>1,2</sup>**

5 <sup>1</sup>Institute of Environment and Sustainable Development, Banaras Hindu University, Varanasi, India

6 <sup>2</sup>DST-Mahamana Centre of Excellence in Climate Change Research, Banaras Hindu University, Varanasi, India

7 <sup>3</sup>High Altitude Cloud Physics Laboratory, Indian Institute of Tropical Meteorology, Pune, India

8 <sup>4</sup>Laboratoire de Physico-Chimie de l'Atmosphère, Université du Littoral Côte d'Opale, Dunkerque, France

9 <sup>5</sup>NASA Ames Research Center, Moffett Field, CA, USA

10 <sup>6</sup>Department of Chemical Engineering and Technology, Indian Institute of Technology (BHU), Varanasi, India

11  
12 *Correspondence to:* Tirthankar Banerjee (tb.iesd@bhu.ac.in; tirthankaronline@gmail.com)

13

**Abstract**

14 The large-scale emissions of airborne particulates from burning of agricultural residues particularly  
15 over the upper Indo-Gangetic Plain (IGP) have often been associated with frequent formation of haze,  
16 adverse health impacts, modification in aerosol climatology and thereby aerosols impact on regional  
17 climate. In this study, short-term variations in aerosol climatology during extreme biomass burning  
18 emissions over IGP, and thereby to regional climate were investigated. Size-segregated particulate  
19 concentration was initially measured and submicron particles (PM<sub>1.1</sub>) were found to dominate  
20 particulate mass within the fine mode (PM<sub>2.1</sub>). Particulate bound water-soluble ions were mainly  
21 secondary in nature, primarily composed of sulfate and nitrate. There was evidence of gaseous NH<sub>3</sub>  
22 dominating neutralization of acidic aerosol species (SO<sub>4</sub><sup>2-</sup>) in submicron particles, in contrast to crustal  
23 dominating neutralization in coarser particulates. Variation in black carbon mass ratio was found to  
24 be influenced by local sources, while sudden increase in concentration was consistent with high Delta-  
25 C, referring to biogenic emissions. Influence of biomass burning emissions were established using  
26 specific organic (levoglucosan), inorganic (K<sup>+</sup> and NH<sub>4</sub><sup>+</sup>) and satellite (UV Aerosol Index, UVAI) tracers.  
27 Levoglucosan was the most abundant within submicron particles (649±177 ng m<sup>-3</sup>), with a very high  
28 ratio (>50) against other anhydrosugars, indicating exclusive emissions from burning of agriculture  
29 residues. Temporal variations of all the tracers were consistent, while NH<sub>4</sub><sup>+</sup> was more closely  
30 associated to levoglucosan. Spatio-temporal distribution of aerosol and few trace gases (CO and NO<sub>2</sub>)  
31 were evaluated using both space-borne active and passive sensors, and a significant increase in  
32 columnar aerosol loading (AOD: 0.98) was evident during extreme biomass burning emissions, with  
33 presence of absorbing aerosols (UVAI > 1.5) having low aerosol layer height (~1.5 km). A strong  
34 intraseasonality in aerosol cross-sectional altitudinal profile was even noted from CALIPSO, referring  
35 dominance of smoke and polluted continental aerosols across IGP. Possible transport mechanism of  
36 biomass smoke was established using cluster analysis and concentration weighted of air mass back-  
37 trajectories. Short-wave aerosol radiative forcing (ARF) was further simulated considering  
38 intraseasonality in aerosol properties, which resulted in considerable increase of atmospheric ARF  
39 (135 Wm<sup>-2</sup>) and heating rate (4.3 K day<sup>-1</sup>) during extreme biomass burning emissions compared to non-  
40 dominating one (56 W m<sup>-2</sup>, 1.8 K day<sup>-1</sup>). We therefore conclude that influence of biomass burning  
41 emissions on regional aerosol climatology must need to be studied in much finer scale to improve  
42 parameterization of aerosol/-climate model across the region.

43



## 1 1. Introduction

2 Aerosols are studied systematically in terms of their potential to influence the transfer of  
3 radiant energy and distribution of latent heat, by which it modifies the Earth's weather and climate.  
4 Aerosols are also associated with nutrient recycling and for governing atmospheric chemistry  
5 (Kanakidou et al., 2018). Aerosol interaction with radiation mainly constitutes its radiative forcing of  
6 climate change (Bellouin et al., 2005; Bond et al., 2013) while, it also modifies the climate by means  
7 of cloud formation processes (Seinfeld et al., 2016). The aerosol-radiation interaction necessitates  
8 understanding on spectrally varying aerosol optical properties, which are associated to particle size  
9 distribution, chemical composition, morphology and mixing states. The representation of aerosol  
10 processes in global/-regional climate models varies considerably and thereby, estimates of aerosol-  
11 radiation interaction still consist significant level of uncertainties (Myhre et al., 2013). This necessitates  
12 extensive regional investigation in terms of aerosol composition and properties for improved  
13 parametrization of aerosol schemes in the regional/-global climate model.

14 The Indo-Gangetic plain (IGP) in South Asia is especially unique in terms of aerosols loading  
15 and diversity that varies over the seasons (Singh et al., 2017a,b; Sen et al., 2017; Sayer et al., 2014;  
16 Kumar et al., 2018). The IGP is often projected to be one of the most vulnerable region in terms of  
17 aerosol induced negative health impacts (Apte et al., 2015) and therefore, numerous observational  
18 and modeling studies were made for better characterization of aerosols (Sen et al., 2017; Moorthy et  
19 al., 2008 and references therein). Recently, Singh et al. (2017a) has concluded the presence of  
20 considerable spatial and seasonal variations in aerosol sources over South Asia, with vehicular  
21 emissions, followed by industrial emissions and secondary aerosols contributing most of the  
22 anthropogenic emissions of fine particulates. However, episodes of specific emissions like from  
23 biomass burning (Wan et al., 2017; Rajput et al., 2011, 2014; Rajput and Sarin, 2014) and use of fire  
24 crackers (Kumar et al., 2016) also induce sudden large-scale changes in aerosol properties, and  
25 necessitate extensive investigation for better representation in regional aerosol model. Post-harvest  
26 agricultural residue burning, especially over upper IGP is projected to release 400 Gg of particulate  
27 bound organic aerosols (OA) and 40 Gg of black carbon (BC, Rajput et al., 2014), almost entirely (90 %)  
28 from burning of rice husks (Rajput et al., 2011). The OA mostly constitute the fine particulate mass  
29 (20-90 %) and are reported to be hydrophilic in nature (Rajput and Sarin, 2014) therefore, pose  
30 potential to act as CCN molecule, or at most compete with sulphate particle (Singh et al., 2017b).  
31 Nevertheless, presence of such huge amount of OA may either lead to reduction in mean evaporation  
32 and modify regional precipitation or may reduce cloud formation processes by inducing additional  
33 heat to the system (Riipinen et al., 2011; Sun and Arriya, 2006). The biomass burning aerosols also  
34 impact the Earth's surface albedo by depositing on glaciers. The net radiative forcing of biomass



1 burning aerosols by aerosol–radiation interactions is close to neutral i.e.  $-0.0$  ( $-0.20$  to  $+0.20$ )  $\text{W m}^{-2}$ ,  
2 having a gradient with negative forcing from OA and positive forcing from BC (Myhre et al., 2013).  
3 Biomass burning aerosols even evolve due to oxidation (Jimenez et al., 2009; Vakkari et al., 2014),  
4 from gas-phase precursors to semi-volatile secondary OA (SOA) and finally to highly volatile oxidized  
5 gases (e.g. CO and  $\text{CO}_2$ ), thus warrants molecular characterization and specific understanding both in  
6 terms of composition, atmospheric chemistry, transport and radiative forcing (Singh et al., 2017b).

7 Several investigations were made to understand the characteristics of biomass burning  
8 aerosols exclusively over IGP. Few attempts were made solely using ground-based information e.g.  
9 aerosol emission budget (Rajput et al., 2014), organic mass-to-organic carbon ratio (Rajput and Sarin,  
10 2014), emissions of PAHs (Rajput et al., 2011), organic molecular tracers (Wan et al., 2017) and  
11 radiative forcing (Sharma et al., 2017; Alam et al., 2011); while few have explored remote sensing  
12 observations to interpret fire (Vadrevu et al., 2012) and aerosol plume characteristics (kaskaoutis et  
13 al., 2014). However, there is a need to integrate both ground and contemporary satellite-based  
14 information so that spatio-temporal characterization of aerosols and its climatic impacts are assessed  
15 more realistically. In the present analysis complementary measurements from both ground and space-  
16 based platforms are therefore combined to trace the vital signatures of extreme biomass burning  
17 emissions, its chemical evolution, transport and aerosol radiative forcing. Initially, chemical  
18 speciations of size-segregated aerosols are made, supported by black carbon dynamics, molecular  
19 tracers of biomass emissions, and further explored in terms of their relevance to regional  
20 meteorology. The spatial extent of aerosol emission and transport was made using Modern-Era  
21 Retrospective Analysis for Research and Applications (MERRA) atmospheric reanalysis data, Global  
22 Data Assimilation System (GDAS) archives and NCEP/ NCAR Reanalysis data. Further, visualization  
23 from ‘A-Train’ satellite constellation, from both space-borne passive sensors like MODerate resolution  
24 Imaging Spectroradiometer (MODIS), Ozone Monitoring Instrument (OMI) and active sensor like  
25 Cloud-Aerosol Lidar and Infrared Pathfinder Satellite Observation (CALIPSO) are included. Briefly, the  
26 results are explored to highlight three exclusive but inter-related mechanisms, i.e. aerosol chemistry,  
27 regional transport and radiative forcing, and their intra-seasonal variations over middle IGP, which  
28 may well be useful for improving aerosol scheme in regional climate model.

## 29 **2 Experimental methods**

### 30 **2.1 Site description**

31 Ground-based aerosol measurements were made at the institutional premises of Banaras  
32 Hindu University, Varanasi ( $25.26^\circ\text{N}$ ,  $82.98^\circ\text{E}$ , 82 m AMSL). The ground station typically experiences  
33 a humid sub-tropical climate, with no localized effects of oceans or mountains (Fig. 1). The



1 predominating wind profile is north-westerly which are projected to subsidize over a section of middle  
2 IGP, coinciding well with the ground monitoring station, thereby facilitates gradual accumulation of  
3 aerosols (Kumar et al., 2018). Interestingly enough, the region also experiences a significant diurnal  
4 variation in atmospheric boundary layer (ABL) associated with high convective turbulence that usually  
5 redistributes aerosols to a greater altitude (Kumar et al., 2015, 2017a). Particulates emitted from  
6 crustal sources, road dust re-suspension, vehicular exhausts and biomass/waste burning are often  
7 reported to primarily constitute the regional aerosol climatology (Singh et al., 2017a).

## 8 **2.2 Micro-meteorology, ABL and wind field**

9 The 24 h average meteorological parameters e.g. temperature, relative humidity (RH) and  
10 wind speed (WS) were obtained from wunderground.com and validated with regional weather  
11 monitoring station data. The ABL heights at specific coordinate were retrieved from Global Data  
12 Assimilation System (GDAS) archives hosted at NOAA-Air Resource Laboratory, which provides  
13 simulated meteorological observations at a gridded scale. The 3-hourly ABL data ( $0.5^\circ$ ) were averaged  
14 on daily basis in parallel to period of particulate measurement. The NCEP/NCAR Reanalysis data was  
15 used to measure the variation of 3-D wind fields at near surface (1000 m) with a horizontal resolution  
16 of  $2.5^\circ \times 2.5^\circ$ . Vector wind composite mean ( $\text{m s}^{-1}$ ) for 925 hPa was plotted for the defined coordinate  
17 ( $6-38^\circ\text{N}$ ,  $50^\circ-105^\circ\text{E}$ ) to understand the synoptic pattern of wind field.

## 18 **2.3 Ground-based measurements**

### 19 **2.3.1 Size-segregated aerosol mass concentration**

20 Size-segregated aerosols were collected on pre-combusted quartz fiber filter using Anderson  
21 eight-stage cascade impactor (Tisch Environmental Inc., USA). Sampling was continued for once in a  
22 week from 1<sup>st</sup> October to 15<sup>th</sup> December 2016, continuously for 72 h (in each week) to get  
23 representative deposition of particulates. The instrument was run with a fix flow rate of 28.3 LPM,  
24 having aerodynamic cut-off diameter of  $<0.43$ ,  $0.65$ ,  $1.1$ ,  $2.1$ ,  $3.3$ ,  $4.7$ ,  $5.8$  and  $>9.0 \mu\text{m}$  (with 50 %  
25 collection efficiency). The individual stages of each sample were then segregated into three groups on  
26 the basis of cut-off diameter (i) coarse mode ( $\text{PM}_{>2.1}$ ) comprising the stages with the aerodynamic  
27 diameter  $>2.1 \mu\text{m}$ ; (ii) fine mode ( $\text{PM}_{1.1-2.1}$ ) for the stages with diameter  $1.1$  to  $2.1 \mu\text{m}$ ; and, (iii)  
28 submicron mode ( $\text{PM}_{<1.1}$ ) for the last two stages with the diameter  $<1.1 \mu\text{m}$ .

### 29 **2.3.2 Black carbon mass concentration**

30 The black carbon (BC) real-time mass concentration was measured using a seven channel  
31 Aethalometer (Model AE-42; Magee Sci. Inc., USA), with a constant flow rate of 3 LPM at 5 minutes  
32 resolution. Aethalometer measures the attenuated beam of light transmitted through aerosol sample



1 on filter tape at seven wavelengths (370, 470, 520, 590, 660, 880 and 950 nm), while attenuation at  
2 880 nm was considered for BC (Bodhaine, 1995). The BC concentration is estimated based on the  
3 concept of linearity between the light attenuation and BC mass deposited on quartz filter. An  
4 absorption efficiency of  $16.6 \text{ m}^2 \text{ g}^{-1}$  (provided by the manufacturer) was used to measure BC after  
5 correction of loading effect. The detailed mechanism for estimation of BC is described in Wang et al.  
6 (2011) and Kumar et al. (2017a). Additionally, BC measured at two wavelengths e.g. 370 nm (indicating  
7 absorption by wood-smoke particles) and 880 nm (by both fossil fuel and wood burning emissions)  
8 were used to compute Delta-C ( $\text{BC}_{370\text{nm}} - \text{BC}_{880\text{nm}}$ ). Delta-C is reported to symbolize smoke emissions  
9 (Wang et al., 2011; Kumar et al., 2016) and therefore, was used as a tracer for biomass emissions.

### 10 2.3.3 Aerosol chemical constituents

#### 11 *Water-soluble ions*

12 The particulate deposits on filter were extracted with deionized water in an ultrasonic bath  
13 (Microclean-109, Oscar, India) for 30 min, and extracts were further filtered through syringe filters  
14 (pore size  $0.2 \mu\text{m}$ ). The water-soluble ionic constituents (WSIC) were analyzed by ion exchange  
15 chromatograph (ICS 3000, Dionex, USA). For measurement of anions ( $\text{Cl}^-$ ,  $\text{NO}_3^-$ ,  $\text{SO}_4^{2-}$  and  $\text{PO}_4^{3-}$ ), the IC  
16 was equipped with a micro-membrane suppressor (AERS-300, 4 mm; Dionex) with IonPac analytical  
17 column (AS11-HC  $\times$  250-mm) connected with a guard column IonPac (AG11-HC,  $4 \times 50\text{mm}$ ; Dionex).  
18 Cations ( $\text{NH}_4^+$ ,  $\text{Na}^+$ ,  $\text{K}^+$ ,  $\text{Mg}^{2+}$ ,  $\text{Ca}^{2+}$ ) were measured through a suppressor (CERS-300, 4 mm; Dionex)  
19 with an analytical column (IonPac CS12A-HC,  $4 \times 250 \text{ mm}$ ; Dionex) and a guard column (IonPac CG11-  
20 HC,  $4 \times 50 \text{ mm}$ ; Dionex, USA). The background contamination was removed by subtracting the blank  
21 filter value from sample values (Kumar et al., 2017b).

#### 22 *Trace metals*

23 The trace metals were extracted from filter discs as per US EPA Method IO-3.2 (EPA, 1999).  
24 The filters were cut into pieces and digested in acid mixture solution (5.55 %  $\text{HNO}_3$  with 16.67 % HCl)  
25 on a hot plate for 2 h. The extracts were filtered, stored at  $4 \text{ }^\circ\text{C}$  and were analyzed by atomic  
26 absorption spectrophotometer (Avanta Ver 2.01, GBC) for Cu, Mn, Fe, Cd, Cr, Pb, Ni, Co, and Zn.

#### 27 *Organic compounds*

28 For determining the aerosol organic constituents, the filter composites of each group were  
29 extracted by ultrasonating the filters initially with dichloromethane-hexane mixture (1:1), followed  
30 by dichloromethane-methanol mixture (1:1). Both solvent extracts were combined and concentrated  
31 using vacuum rotatory evaporator and nitrogen evaporator to a volume of  $100 \mu\text{L}$  (Hu et al., 2013).  
32 The extracts were derivatized by silylation with N, O-bis-(trimethylsilyl)-trifluoroacetamide and 1 %



1 trimethylchlorosilane prior to analysis. After derivatization, the residue was re-dissolved in hexane  
2 and analyzed by gas chromatography-mass spectrometry (GCMS-QP2010 Ultra, Shimadzu, Japan)  
3 equipped with Rxi-5MS fused silica capillary column having dimension 30 m x 0.25 mm id x 0.25  $\mu$ m  
4 (Restek, Bellefonte, PA, USA). The 1  $\mu$ L of samples were injected in GCMS at 260°C injector  
5 temperature in splitless mode. The column oven temperature program was started at 50°C with 2 min  
6 of the isothermal hold which further raised up to 120 °C (linear elevation @ 30 °C min<sup>-1</sup>) and 300 °C  
7 (linear elevation @ 6 °C min<sup>-1</sup>) followed by the isothermal hold of 11 min. The electron impact  
8 ionization was used to produce molecular ions at 70 eV with the ion source and interface temperature  
9 of 230 °C and 270 °C, respectively. The molecular ions were scanned for a wide range of m/z from 40  
10 to 650. The target compounds were identified on the basis of retention time and fragmentation  
11 pattern from National Institute of Standards and Technology (NIST) library and standard solutions of  
12 analytes.

## 13 **2.4 Satellite-based observations**

### 14 **2.4.1 Aqua/-Terra MODIS data**

15 The aerosol optical depth (AOD) at 550 nm was retrieved daily from MODIS onboard Aqua  
16 satellite in parallel to ground-based aerosol monitoring. The level 2 Collection 6 AOD at 10 km  
17 resolution was retrieved using MODIS merged DT-DB AOD (AOD\_550\_  
18 Dark\_Target\_Deep\_Blue\_Combined, Levy et al., 2013). The selection of merged DT-DB for retrieving  
19 AOD was based on higher retrieval number and accuracy across the IGP (Mhawish et al., 2017). The  
20 AOD for the ground station was calculated as the average of 5 x 5 pixels, around the monitoring site.  
21 Angstrom exponent (AE,  $\alpha$ ) was retrieved using MODIS C6 level 2 DB AOD and relation between AOD  
22 and AE was used to measure the aerosol loading and the particle size (Kumar et al., 2015; Mhawish et  
23 al., 2017). Columnar water vapor content (CWV) was retrieved from Aqua MODIS collection 6 level 2  
24 infrared channel at 1km spatial resolution. To illustrate the impact of biomass burning, the fire spots  
25 were retrieved over the IGP from Aqua/-Terra MODIS Fire Mapper product (collection 6, spatial  
26 resolution 1x1 km<sup>2</sup>) provided by the Fire Information for Resource Management System (FIRMS,  
27 <https://firms.modaps.eosdis.nasa.gov>). The details about MODIS fire products and its algorithm may  
28 be found elsewhere (Justice et al., 2006).

### 29 **2.4.2 Aura-OMI and MERRA-2 reanalysis data**

30 The OMI onboard AURA satellite has a typical daily global coverage with 13 x 24 km<sup>2</sup> spatial  
31 resolution at nadir and measures solar backscatter irradiation in the UV-visible spectrum (264-504  
32 nm; Levelt et al., 2006). Ultraviolet Aerosol Index (UVAI), tropospheric NO<sub>2</sub>, total columnar ozone  
33 (TCO) and Single scattering albedo (SSA) were retrieved from Aura OMI available at NASA Goddard



1 Earth Sciences Data and Information Services Centre (GES DISC). Aura OMI UVAI is capable of detecting  
2 aerosol absorption from satellite measured radiances without any prior assumption on aerosol  
3 composition (Torres et al., 2013). It is a qualitative parameter and is widely used to identify the UV  
4 absorbing aerosols (e.g. smoke plumes, soot and mineral dust; Torres et al., 2013; Mhawish et al.,  
5 2018). The UVAI based on OMI near-UV aerosol retrieval algorithm (OMAERUV) was extracted from  
6 Level 2G, version 003 aerosol product containing one day's Level 2 data set of original pixels ( $13 \times 24$   
7  $\text{km}^2$ ) into  $0.25^\circ \times 0.25^\circ$  grids. The  $\text{NO}_2$  tropospheric column density was retrieved from cloud screened  
8 (cloud fraction  $<30\%$ ) Level 3, version 003, daily  $0.25^\circ \times 0.25^\circ$  gridded OMNO2d product (Krotkov et  
9 al., 2017). To estimate TCO, Level 3e data (OMDOAO3) at a spatial resolution of  $0.25^\circ \times 0.25^\circ$  was used.  
10 SSA at 550 nm was retrieved from OMI level 2G product (OMAERUV) at  $0.25^\circ \times 0.25^\circ$  resolution. The  
11 Carbon Monoxide (CO) surface concentration (in ppbv) was retrieved from Modern-Era Retrospective  
12 Analysis for Research and Applications, version 2 (MERRA-2) atmospheric reanalysis data available at  
13  $0.5^\circ \times 0.625^\circ$  from GES DISC.

#### 14 **2.4.3 CALIPSO-CALIOP observations**

15 CALIPSO products were used to examine the vertical distribution of aerosols, altitude of  
16 aerosol layers, clouds, aerosol types and their properties at visible (532nm) and near-IR wavelengths  
17 (1064 nm). The V4.10 CALIOP Level 2 altitude-orbit cross-section profiles obtained from CALIPSO sub-  
18 setting web application (<https://www-calipso.larc.nasa.gov>) was used. The Lidar profiles were  
19 processed for images of vertical feature masks, aerosol subtypes and extinction coefficients (at 532  
20 nm) at 30 m vertical resolution over the selected grid ( $80^\circ$ - $86^\circ$  N and  $22^\circ$ - $28^\circ$  E). The details about data  
21 products, calibration and uncertainty are discussed in Rogers et al. (2011).

#### 22 **2.5 Air-mass back trajectory**

23 The NOAA HYSPLIT model (Draxler and Rolph, 2003) was used to simulate particle back  
24 trajectories in a three-dimensional system. The HYSPLIT was run on using the Global Data Assimilation  
25 System data (GDAS,  $0.5^\circ \times 0.5^\circ$ ) available from archive dataset (<http://ready.arl.noaa.gov/gdas1.php>)  
26 to predict 120 h air-mass back trajectories (00:00, 06:00, 12:00 and 18:00 UTC) starting from October  
27 to December 2016. Trajectories for different aerosol loading periods were then overlaid on MODIS  
28 fire map to study the transboundary movement of emissions from biomass burning. The trajectory  
29 analysis was made using GIS-based software TrajStat (Wang et al., 2009). Concentration weighted  
30 trajectories (CWT) were also drawn considering columnar aerosol loading to evaluate potential  
31 aerosol source fields and mechanism of aerosol transport over the Gangetic plain. The specificities of  
32 the models' parameters and algorithms are detailed elsewhere (Wang et al., 2009; Kumar et al., 2018).

33



## 1    **2.6 Aerosol optical properties, radiative forcing and heating rate**

2            Aerosol induced shortwave (0.2–4.0  $\mu\text{m}$ ) direct radiative forcing (ARF) was estimated using  
3    Santa Barbara DISORT Atmospheric Radiative Transfer (SBDART) model (Ricchiuzzi et al., 1998). The  
4    SBDART estimates plane-parallel radiative transfer in a clear sky condition for both Earth's top of the  
5    atmosphere (TOA) and at the surface (SUF), while atmospheric forcing (ATM) is calculated as the  
6    difference between them. The standard atmospheric profile is used together with input variables e.g.  
7    AOD, SSA, CWV, TCO and asymmetry parameter (ASP) derived through OPAC model (Optical  
8    Properties of Aerosols and Clouds; Hess et al., 1998). The OPAC provides aerosol optical properties  
9    over a wide range of wavelength and delivers necessary input to SBDART. Mean mass concentrations  
10   of aerosol water soluble (WSIC) and insoluble (dust and organics) components along with BC mass  
11   concentrations were converted to particle number densities and introduced to OPAC for deriving  
12   aerosol optical properties. The OPAC derived outputs were tuned in respect to measured relative  
13   humidity. The AOD and SSA were further reconstructed to match modelled and satellite derived values  
14   within  $\pm 5\%$  deviation.

15            The weekly mean values of AOD, SSA, ASP, CWV, TCO, visibility and AE were included as an  
16   input to SBDART. The SBDART includes multiple scattering in a vertically inhomogeneous, non-  
17   isothermal plane-parallel media, and is reported to be efficient in resolving the radiative transfer  
18   equation (Raju et al., 2016). The ARF was calculated using 10 solar zenith angles (0 to 89, with  
19   increment of 10) and proceed for conditions like 'with aerosols' or 'without aerosols'. The surface  
20   albedo was decided based on visual observation considering a combination of snow, ocean, sand and  
21   vegetation. Overall uncertainty in the estimated ARF was in the range of 10–15 % (Alam et al., 2011).  
22   The ATM-ARF was further used to compute aerosol atmospheric heating rate ( $\partial T/\partial t$ ,  $\text{K day}^{-1}$ ), using  
23   equation (1):

$$24 \quad \partial T/\partial t = (g/C_p) * (\Delta F/\Delta P) \quad (1)$$

25   where  $\Delta P$  is the difference in forcing,  $\Delta P$  is the pressure difference between top and bottom boundary  
26   layer,  $C_p$  is specific heat capacity of air at constant pressure and  $g$  is the acceleration due to gravity  
27   (Kumar et al., 2017a).

## 28    **3. Results and discussion**

### 29    **3.1 General characteristics of aerosols**

30            The weekly variation in particulate concentrations in different size fractions are presented in  
31   Fig. 2 with the descriptive statistics in Table S1. The total aerosol mass concentrations have high intra-  
32   seasonal variations (median: 370; range: 134–734  $\mu\text{g m}^{-3}$ ), mainly influenced by coarse mode particles





1 (PM<sub>>2.1</sub>) contributing 63±15 % of particulate mass. In contrast, contribution of submicron (PM<sub><1.1</sub>:  
2 27±12 %) and fine mode particles (PM<sub>1.1-2.1</sub>: 10±4 %) to total aerosol loading were relatively less  
3 (<37%). The average (±1σ) mass concentration of PM<sub>2.1</sub> (PM<sub><1.1</sub> + PM<sub>1.1-2.1</sub>) and total aerosol loading  
4 was 162 (±123) and 390 (±199) μg m<sup>-3</sup>, which were approximately 98 % (against PM<sub>2.5</sub>) and 92 % higher  
5 compared to annual averages observed over the monitoring station (Murari et al., 2017; Prajapati and  
6 Tripathi, 2008). To our knowledge, there are no published reports on submicron particle concentration  
7 over the ground station. Time-series analysis of size-segregated particulates (Fig. 2) indicate the  
8 submicron (PM<sub><1.1</sub>) and fine mode particles (PM<sub>1.1-2.1</sub>) only had a late rise in mass concentrations, while  
9 the coarse mode particulates (PM<sub>>2.1</sub>) did not show any trend. However, there was a definite increasing  
10 pattern in fine to coarse particle ratio (PM<sub>2.1</sub>/PM<sub>>2.1</sub>; mean: 0.7±0.5; range: 0.2-1.5), due to a  
11 continuous increase of the fine mode from mid-November to the end of the monitoring. Thus the  
12 contribution of fine mode particle to total aerosol loading increased from mid-November (>40 %), and  
13 contributed almost 60 % of particulate mass during the month of December. The submicron particles  
14 also indicate a high median concentration (96 μg m<sup>-3</sup>) compared to fine mode (33 μg m<sup>-3</sup>), and the  
15 particle ratio (PM<sub><1.1</sub>/PM<sub>1.1-2.1</sub>) remain >1 throughout, only to exceed values >2.5 from November to  
16 December. This clearly indicates the dominance of submicron particles within fine mode fractions,  
17 possibly associated to anthropogenic emissions, and also influenced by local meteorological  
18 conditions e.g. low temperature (mean±SD: 20±3 °C), calm wind (mean: 0.6 m s<sup>-1</sup>) and shallow  
19 boundary layer height (mean±SD: 379±89 m).

## 20 3.2 Aerosol chemical speciations

### 21 3.2.1 Water soluble inorganic species (WSIS)

22 Temporal variation of WSIS in size-segregated airborne particulates are presented in Fig. 3a.  
23 It indicates the major contribution of WSIS to submicron (21 %) and fine particle mass (21 %) compared  
24 to coarser particles (13 %). The secondary inorganic aerosols (SIA = SO<sub>4</sub><sup>2-</sup> + NO<sub>3</sub><sup>-</sup> + NH<sub>4</sub><sup>+</sup>) together  
25 accounted for 17 % of the submicron particle mass, with major contributions from sulfate (9%) and  
26 nitrate (6 %). Similar was the case for fine particulates as SIA contributed to almost 17 % of aerosol  
27 mass with predominate contribution from sulfate (8 %) and nitrate (6 %), and a relatively small  
28 proportion of ammonia (4 %). In contrast, the relative contribution of SIA to coarse particulate was  
29 lower (7 %), also primarily associated to sulfate (5 %) and nitrate compounds (2 %). This indicates the  
30 secondary nature of origin of fine and submicron particles which possibly evolve through gas-phase  
31 photochemical conversion of SO<sub>2</sub> and NO<sub>2</sub>, eventually neutralized by crustal species like carbonate  
32 salts (CaCO<sub>3</sub> and MgCO<sub>3</sub>) associated with the airborne dust (Murari et al., 2015, 2016). The time-series  
33 of SIA contribution to particulate mass (Fig. 3a) indicate a dominance (although in different extent) of  
34 secondary aerosols in PM<sub>1.1-2.1</sub> and PM<sub>>2.1</sub> only during November.



1           Among the WSIS,  $\text{SO}_4^{2-}$  was invariably the most abundant within each particulate size fraction  
2 ( $\text{PM}_{<1.1}$ : 39 %,  $\text{PM}_{1.1-2.1}$ : 32 %,  $\text{PM}_{>2.1}$ : 36 %), followed by  $\text{NO}_3^-$  ( $\text{PM}_{<1.1}$ : 27 %,  $\text{PM}_{1.1-2.1}$ : 29 %,  $\text{PM}_{>2.1}$ : 17  
3 %). The  $\text{NO}_3^- / \text{SO}_4^{2-}$  ratio was considered as an indicator of the mobile and stationary sources of  
4 nitrogen and sulfur (Tian et al., 2016). An average ratio varying from 0.62 to 1.92 was noted for all  
5 size-segregated particulates testifying dominance of both sources, although in different time-scales.  
6 In later phase, the ionic ratio ( $\text{NO}_3^- / \text{SO}_4^{2-}$ ) enhanced ( $>1$ ) in submicron and fine mode particles, well  
7 identical to the reported haze events over Guangzhou (Tan et al., 2009) and Suzhou, China (Tian et al.,  
8 2016). A very high  $\text{NO}_3^- / \text{SO}_4^{2-}$  ratio ( $3.2 \pm 1.3$ ) was only noted in fine aerosols during October, mainly  
9 due to lower concentration of sulphate. The next two dominant contributors to WSIS were  $\text{NH}_4^+$   
10 ( $\text{PM}_{<1.1}$ : 14 %,  $\text{PM}_{1.1-2.1}$ : 19 %,  $\text{PM}_{>2.1}$ : 5 %) and  $\text{K}^+$  ( $\text{PM}_{<1.1}$ : 8 %,  $\text{PM}_{1.1-2.1}$ : 5 %,  $\text{PM}_{>2.1}$ : 2 %), both considered  
11 as a molecular tracer for biogenic emission (Banerjee et al., 2015). They constitute the greater  
12 proportion of WSIS in  $\text{PM}_{<1.1}$  and  $\text{PM}_{1.1-2.1}$ , especially from last week of October till the end of  
13 November, signifying elevated contribution of biomass/ agro-residue burning emissions to these  
14 particle sizes. Further, a strong correlation ( $R^2=0.9$ ) between  $\text{NH}_4^+$  and  $\text{SO}_4^{2-}$  and high  $\text{NH}_4^+/\text{SO}_4^{2-}$   
15 equivalent ratio ( $0.9 \pm 0.2$ ) in submicron particulates indicate the abundance of gaseous  $\text{NH}_3$  to  
16 neutralize acidic species ( $\text{SO}_4^{2-}$ ) by forming  $(\text{NH}_4)_2\text{SO}_4$  and/or  $\text{NH}_4\text{HSO}_4$ . The  $\text{NH}_4^+/\text{SO}_4^{2-}$  equivalent ratio  
17 gradually increased from week 5 (mean: 1.2, range: 0.9-1.3), possibly due to abundant emission of  
18  $\text{NH}_4^+$  from biomass emissions. Unlike submicron particles, the low  $\text{NH}_4^+/\text{SO}_4^{2-}$  equivalent ratios ( $<0.7$ ,  
19 mean: 0.4) in coarse mode particles indicate the predominant neutralization by crustal minerals  
20 instead of  $\text{NH}_3$ .

21           Unlike the other WSIS,  $\text{Na}^+$  and  $\text{Ca}^{2+}$  were found to contribute maximum in  $\text{PM}_{>2.1}$  ( $\text{Na}^+$ : 2 %;  
22  $\text{Ca}^{2+}$ : 3 %), referring their crustal origin. The relative abundance of  $\text{Cl}^-$  in size-segregated aerosols was  
23 roughly equal for each size fraction, contributing almost in identical to total WSIS in  $\text{PM}_{<1.1}$  (6 %),  $\text{PM}_{1.1-}$   
24  $2.1$  (5 %) and  $\text{PM}_{>2.1}$  (4 %). The possible origin of  $\text{Cl}^-$  in  $\text{PM}_{>2.1}$  could be the aged sea salt, transported  
25 from Bay of Bengal, but its association with  $\text{PM}_{<1.1}$  was most likely due to biomass burning emissions  
26 (Pavuluri et al., 2011; Murari et al., 2015). The temporal variations of WSIS in all particulate size  
27 fractions were consistent except for  $\text{Mg}^{2+}$  and  $\text{PO}_4^{3-}$  with a contribution of both ions to particulate  
28 masses less than 0.2 %, indicating their non-biomass specific emission. A strong correlation was noted  
29 between the anion and cation equivalents within all the groups (0.7-0.9) indicating that maximum ions  
30 were from the filter samples. The total ion equivalent ratio (anions to cation) refer a cationic imbalance  
31 ( $\text{PM}_{<1.1}$ : 1.2,  $\text{PM}_{1.1-2.1}$ : 0.8 and  $\text{PM}_{>2.1}$ : 0.6) with excess cations in fine and coarse mode particles,  
32 possibly due to unmeasured components like carbonates and bicarbonates.

### 33 3.2.2 Trace metals



1 Total metallic contribution to particulate mass was found maximum in  $PM_{1.1-2.1}$  (24 %),  
2 followed by  $PM_{>2.1}$  (11 %) and least in  $PM_{<1.1}$  (7 %, Fig. 3b). The most abundant elements were Na, Ca,  
3 K and Zn for all size fractions, contributing 90-98 % of total identified metals, while the remaining  
4 fractions were primarily constituted by Fe (1-10 %). Within the detectable level of metals, Ca and Na  
5 share 88 % of metal concentrations in  $PM_{<1.1}$ , contributing 7% of submicron particulate mass, without  
6 having any specific temporal trend. However, Ca, Na were found high in  $PM_{1.1-2.1}$  (Ca: 10 %; Na: 7 %),  
7 referring their origin from resuspension of crustal materials and road dust.

8 There are some evidences of trace metal emissions from burning of biomass. Wang et al.  
9 (2015) have concluded biomass combustion as the most prominent source of Fe concentration for  
10 submicron particles. For this analysis, although Fe was measured maximum in  $PM_{>2.1}$ , the relative  
11 increase in Fe concentration in submicron ( $PM_{1.1}$ : 59 %) and fine aerosols ( $PM_{1.1-2.1}$ : 415 %) during week  
12 6 to week 9 possibly indicate the added contribution of biomass burning emissions. Beside Fe, there  
13 are also reports of trace metals emissions particularly K, Cu, S, Zn, Pb from burning of rice-straw (Ryu  
14 et al., 2012); organic bound  $Fe^{2+}$ ,  $Cu^{2+}$ ,  $Ni^{2+}$ ,  $Zn^{2+}$  from hardwood burning (Chang-Graham et al., 2011)  
15 and Cu, Pb, Ni, As from the burning of biomass fuel (Zhang 2014). In our case, massive increase in K  
16 ( $PM_{1.1}$ : 528 %;  $PM_{1.1-2.1}$ : 119 %) was noted between week 6 and week 9. This contrasted with coarse  
17 particle bound Fe and K which are primarily of crustal origin (Banerjee et al., 2015), and recorded 15  
18 % (Fe) and 83 % (K) increase in concentration within week 6 to 9. Zinc was found considerably high in  
19  $PM_{>2.1}$  (3 %) and relatively small proportion in  $PM_{1.1-2.1}$  (2 %). The major sources of atmospheric Zn are  
20 burning of residual oil, refuse and garbage (Gonzalez et al., 2016) which possibly leads to higher mass  
21 fractions in coarser particulates. Even, a relatively high Zn concentration was noted irrespective of  
22 particulate size in later phase of monitoring coincide with the winter specific burning of waste/- refuse  
23 over the region (Kumar et al., 2017b). The relative contribution of rest of the trace metals (e.g. Mn,  
24 Pb, Cd, Ni, Cu, Cr and Co) in particulate mass were insignificant (<0.05 %), without having any specific  
25 temporal pattern.

### 26 3.3 Characteristics of BC mass loading

27 Daily average BC concentration and Delta-C ( $BC_{370} - BC_{880}$ ) are plotted in Fig. 4 with some data  
28 gaps. The 24 h average BC concentration varied from 2.0-15.4  $\mu g m^{-3}$  with a seasonal mean ( $\pm 1\sigma$ ) of  
29 8.3 ( $\pm 2.9$ )  $\mu g m^{-3}$ . The season specific BC average was 80 % higher in comparison to annual mean  
30 reported over the ground station (4.6  $\mu g m^{-3}$ ; Kumar et al., 2017a), while there are also reports of  
31 winter-specific very high BC mixing ratio (22  $\mu g m^{-3}$ ; Murari et al., 2016) that usually persist over the  
32 region. Over middle IGP, vehicular exhausts mainly regulate the BC profile (Kumar et al., 2016, 2017a;  
33 Murari et al., 2016), while isolated cases like large-scale burning of agriculture residues/ biomass/  
34 waste and emissions from residential heating also contribute in BC concentrations (Kumar et al.,



1 2017b). The hourly BC profile indicates a distinct diurnal profile with a general trend of high  
2 concentration ( $>9 \mu\text{g m}^{-3}$ ) during night to early morning hours (21:00-7:00 h), and a low concentration  
3 ( $<6 \mu\text{g m}^{-3}$ ) during day time (11:00-17:00 h). A gradual rise in BC in morning and evening hours well  
4 coincide with the traffic rush hours, indicating the contributions of traffic emissions. However, the rest  
5 of BC diurnal profile is mainly attributed to the variation in boundary layer height, which otherwise  
6 considered as the most important factor in regulating BC after the source itself (Kumar et al., 2016,  
7 2017a).

8 The temporal plot shows an enhanced BC concentration from the end of October (week 4) till  
9 the November end (week 9) possibly due to increased source strength, in addition to the influence of  
10 local meteorology. While there was no significant variation in meteorological variables within this  
11 timeframe (Table S1), we hypothesize that the variation in BC source strength might have well  
12 influenced the BC concentration. To understand the variation in BC sources, 24 h average Delta-C  
13 concentration (mean $\pm$ SD:  $2.3\pm 1.0 \mu\text{g m}^{-3}$ ) is also included in Fig. 4, which refers a temporal shift in BC  
14 sources. Except few exceptions, high Delta-C ( $>2.3 \mu\text{g m}^{-3}$ ) was observed particularly in the month of  
15 November (80 % of days) and December (46 %), referring added contribution of biomass burning  
16 emissions.

### 17 3.4 Composition of organic aerosols

18 Size-segregated particle-bound organic aerosols (OA) were analysed for 22 *n*-alkanes ( $\text{C}_{13}$ - $\text{C}_{34}$ ),  
19 3 anhydrosugars (levoglucosan, mannosan and galactosan), 4 PAHs and 10 *n*-alkanoic acids ( $\text{C}_{12}$ - $\text{C}_{26}$ )  
20 (Fig. 5). Considerable variation in the concentration and size distributions of these OA were  
21 noted. Contributions of OA to size-segregated particulates were relatively less because of partial  
22 characterization through GC-MS. Among the identified species, *n*-alkanes were invariably the highest  
23 within  $\text{PM}_{<1.1}$  (mean $\pm$ SD:  $484\pm 103 \text{ ng m}^{-3}$ ) compared to fine ( $267\pm 43 \text{ ng m}^{-3}$ ) and coarse mode aerosols  
24 ( $308\pm 93 \text{ ng m}^{-3}$ ). The molecular distribution of *n*-alkanes homologues in all three size fractions showed  
25 a slight dominance of odd-numbered *n*-alkanes. The CPI (Carbon Preference Index) remain close to  
26 unity (CPI range: 1.2-2.1; mean $\pm$ SD:  $1.5\pm 0.5$ ), indicating dominance of anthropogenic emissions like  
27 combustion of fossil fuels and biomass burning. The higher molecular weight homologues ( $>\text{C}_{25}$ )  
28 concentration were found highest in  $\text{PM}_{<1.1}$  with an oscillating pattern, having odd molecules  
29 concentration higher than the adjacent even molecules (Fig. 5b). In contrast the low molecular weight  
30 homologues ( $<\text{C}_{25}$ ) showed no such specific pattern of odd/even dominance. The sources of higher  
31 homologues ( $\text{C}_{27}$ ,  $\text{C}_{29}$  and  $\text{C}_{31}$ ) are probably the surface deposited plant litter for coarse mode and  
32 biomass burning for fine mode aerosols, while low molecular weight homologues ( $<\text{C}_{25}$ ) primarily  
33 originate from the fossil fuel combustion (Kang et al., 2016). Saturated fatty acids were found to  
34 constitute a larger fraction of solvent extractable organics within coarse mode ( $439\pm 38 \text{ ng m}^{-3}$ )



1 and submicron particles ( $357 \pm 162 \text{ ng m}^{-3}$ ) in comparison to fine mode ( $171 \pm 57 \text{ ng m}^{-3}$ ). For all three  
2 size fractions, total low molecular weight fatty acids ( $\leq C_{20}$ ) concentration was found higher than the  
3 high molecular weight fatty acids ( $\geq C_{20}$ ), indicating the anthropogenic emissions like vehicular,  
4 residential biomass burning and energy practices. Presence of high concentration of  $C_{12}$ , and  $C_{15}$  refer  
5 the dominance of cooking oil combustion. The high concentration of  $C_{22}$  further suggests the influence  
6 of biomass burning which potentially emit both, high and low fatty acids (Mochida et al., 2007). The  
7 fatty acid amide was found in trace amount which could possibly be derived from fatty acid and  
8 ammonia during burning process. Presence of PAHs were comparatively less, primarily within  
9 submicron particles which were mainly emitted from incomplete combustion of wood, oils and coal.

10 Levoglucosan was found to be the most abundant in the submicron particles with an average  
11 ( $\pm 1\sigma$ ) of  $649 (\pm 177) \text{ ng m}^{-3}$ . In contrast, concentration in fine ( $229 \pm 87 \text{ ng m}^{-3}$ ) and coarse particles  
12 ( $162 \pm 68 \text{ ng m}^{-3}$ ) levoglucosan concentrations were relatively low, referring the dominating influence  
13 of burning emissions in submicron particles. Levoglucosan concentration measured in this study are  
14 well comparable to other reported observations, especially with the cases that have accounted the  
15 influence of biomass burning emissions e.g. New Delhi ( $1978 \text{ ng m}^{-3}$ , Li et al., 2014), Mt. Tai, China ( $391$   
16  $\text{ ng m}^{-3}$ , Fu et al., 2008), Gent, Belgium ( $477 \text{ ng m}^{-3}$ , Zdrahal et al., 2002), Lumbini, Nepal ( $734 \text{ ng m}^{-3}$ ,  
17 Wan et al., 2017) and Beijing, China ( $590 \text{ ng m}^{-3}$ , Cheng et al., 2013). Beside levoglucosan, relative  
18 concentration of other anhydrosugars (mannosan and galactosan) in all size-segregated aerosols were  
19 negligible ( $< 70 \text{ ng m}^{-3}$ , not shown).

### 20 3.5 Signature of biomass burning emissions

21 Biomass primarily consists of different bio polymers (e.g. cellulose, hemicellulose, lignin,  
22 suberin, sporopollenin and chitin) with small proportion of lipids and terpenoids. During thermal  
23 combustion, such biomass emits different types of organic molecules, some of which has the potential  
24 to be considered as signature molecule based on their long residence time and chemical stability  
25 (Banerjee et al., 2015). The major combustion product of cellulose and hemicellulose includes  
26 anhydrosugars like levoglucosan (1,6-anhydro- $\beta$ -D-glucopyranose,  $C_6H_{10}O_5$ ) and its two isomers  
27 (mannosan and galactosan). Among these, levoglucosan is a robust and widely used tracer for biomass  
28 burning emissions, both globally (Simoneit et al., 1999; Schkolnik et al., 2005; Cheng et al., 2013), and  
29 over IGP (Li et al., 2014; Banerjee et al., 2015; Wan et al., 2017). In our case, levoglucosan was  
30 abundant in submicron particles with a peak during November (week 6 to 9, Fig. 6). The rise in  
31 concentration was universal in each particulate size fractions, but typically in submicron ( $837 \pm 83$   
32  $\text{ ng m}^{-3}$ ) and fine particulates ( $311 \pm 47 \text{ ng m}^{-3}$ ), having 54-70 % rise against rest of the monitoring period.  
33 This could correspond to a short-term variation in emissions source strength which possibly have well  
34 influenced the regional aerosol property. A ratio between levoglucosan with rest of the anhydrosugars



1 was also considered to indicate the dominating type of biomass burning, with a ratio <10 specific for  
2 softwood combustion, and >10 for burning of hardwood and crop residues (Cheng et al., 2013). Even  
3 a ratio >40 was reported from physical experiments using rice straw, wheat straw and maize stalks  
4 (Engling et al., 2009). Although, the presence of mannosan and galactosan was not frequent in our  
5 case, but an overall ratio >50 refers the exclusive dominance of agriculture residue burning across the  
6 IGP.

7 The possibility of considering  $K^+$  and  $NH_4^+$  as biomass burning tracers were investigated in  
8 terms of their association with levoglucosan for submicron and fine particulates. In general, the  
9 temporal trend of levoglucosan coincided well with both  $K^+$  and  $NH_4^+$ , and all these tracers registered  
10 a gradual rise in concentration during November. Highly significant correlation ( $R^2$ ) between  
11 levoglucosan and  $K^+$  ( $PM_{1.1}$ : 0.80,  $PM_{1.1-2.1}$ : 0.76;  $p < 0.01$ ), and levoglucosan and  $NH_4^+$  ( $PM_{1.1}$ : 0.95,  $PM_{1.1-2.1}$ : 0.60;  $p < 0.01$ ) were noted at 99 % confidence interval. That definitely indicates that levoglucosan,  
13  $K^+$  and  $NH_4^+$  have similar biogenic sources over IGP which predominately contribute to the aerosol  
14 loading, especially in  $PM_{1.1}$  and  $PM_{1.1-2.1}$ . The relation between levoglucosan with  $K^+$  and  $NH_4^+$  further  
15 appeared to be non-linear, with an exponential fit for submicron ( $R^2$ : 0.84, 0.94) and for fine  
16 particulates ( $R^2$ : 0.83, 0.65). Non-linear correlations between levoglucosan and  $K^+$  are also reported at  
17 Amazon (Schkolnik et al., 2005) and in Beijing (Cheng et al., 2013) during extreme biomass burning  
18 emissions. There was also evidence that  $NH_4^+$  was better associated with levoglucosan compared to  
19  $K^+$ , referring the presence of additional  $K^+$  sources across the region (like fireworks, Kumar et al., 2016).  
20 However, in absence of aerosol organic carbon content, contribution of biomass burning to aerosol  
21 mass was not computed.

22 Besides using conventional biomass burning tracers, we also evaluated the association of  
23 submicron and fine particulate bound levoglucosan with weekly averages of Delta-C and UVAI (Fig. 6).  
24 Both Delta-C and UVAI are the measures of identifying the relative dominance of absorbing aerosols  
25 in the environment. In all scenarios, significant correlation ( $R^2$ ) was noted between levoglucosan with  
26 Delta-C (0.65,  $p < 0.01$ ) and UVAI (0.66,  $p < 0.01$ ). In addition to the ground-based aerosol measurement,  
27 dynamic profile of trace gases concentration, especially for those that behave as aerosol precursors,  
28 are assessed from Real-time Air Quality Data inventory of Central Pollution Control Board  
29 (<https://app.cpcbcr.com/ccr>). The hourly average concentrations of individual trace gases were  
30 initially checked for data quality and outliers, and further averaged to 24 h. No such universal trend in  
31 concentration of all the trace gases was evident, except an overall increasing trend for NO, NO<sub>2</sub>, NO<sub>x</sub>,  
32 and CO, while SO<sub>2</sub> remained stable and there was a negative trend for O<sub>3</sub>. The most striking feature in  
33 the abundance of all the trace gases was to have an increase in concentration particularly during  
34 November, although of different magnitude. This was also evident in the variation of particulate



1 bound biomass tracers, which inspire us to consider two different aerosol loading scenarios e.g.  
2 scenario 1 for biomass burning dominating period (week 6 to 9, BDP) and scenario 2 for biomass  
3 burning less dominant period (week 1-5 and week 10-11, BLDP). Such classification was intended to  
4 recognize if there is any variation in aerosol source fields over IGP and in aerosol-induced radiative  
5 forcing.

### 6 **3.6 Spatio-temporal nature of aerosol columnar properties**

7 Spatio-temporal variations in aerosol columnar properties and trace gases are plotted in Fig.  
8 7a, including the daily variations at the ground station (Fig. 7b). Instead of considering the columnar  
9 properties for the entire season, spatial plots are generated for two different scenarios like BDP and  
10 BLDP.

11 The spatial pattern in aerosol columnar properties was typical having a very high aerosol  
12 loading exclusively over IGP (area weighted AOD mean $\pm$ SD:  $0.55\pm 0.21$ ) in comparison to the rest of  
13 South Asia ( $0.31\pm 0.21$ ). However, there was no such temporal variation particularly over IGP as both  
14 BDP<sub>AOD</sub> ( $0.56\pm 0.23$ ) and BLDP<sub>AOD</sub> ( $0.53\pm 0.23$ ) was almost similar. The BDP<sub>AOD</sub> was slightly higher (12 %  
15 to that of reported decadal average ( $0.50\pm 0.25$ , Kumar et al. 2018), and was comparable to the season  
16 specific average over IGP ( $0.55\pm 0.20$ ; Kumar et al., 2018). It should be noted that area weighted AOD  
17 average includes all the pixels retrieved across the region, some of which may not represent the  
18 biomass emissions. This leads us to further retrieve and compare AOD particularly over the ground  
19 station. In this case, the mean AOD was significantly high during post-monsoon ( $0.81\pm 0.39$ ), 44 %  
20 higher for BDP<sub>AOD</sub> ( $0.98\pm 0.42$ ) in respect of BLDP<sub>AOD</sub> ( $0.68\pm 0.32$ ). Even, the BDP<sub>AOD</sub> was 46 % higher  
21 compared to decadal average for the station ( $0.67\pm 0.28$ ; Kumar et al., 2018). Figure 7a also includes a  
22 comparison of relative dominance of aerosol types in terms of AE, and in both conditions fine particles  
23 (AE; BDP: 1.5, BLDP: 1.7) were found to dominate with a season specific mean ( $\pm 1\sigma$ ) of  $1.6 (\pm 0.2)$ .

24 Following the evidence of persisting high AOD and high AE indicating the dominance of fine  
25 particulates of anthropogenic origin, the nature of aerosols in terms of absorbing and/or scattering  
26 was distinguished through satellite observation. OMI UVAI has been widely applied to detect dust  
27 (Badarinath et al., 2010), biomass burning aerosols (Torres et al., 2013; Kaskaoutis et al., 2014) and  
28 soot particles (Kumar et al., 2016), and has also been used in combination with CALIPSO to detect  
29 height of aerosol layer (Guan et al., 2010). In our experiment, the daily UVAI varied from (-) 0.34 to (+)  
30 2.24 with a seasonal mean ( $\pm 1\sigma$ ) of  $0.99 (\pm 0.49)$  over IGP, which is considerably higher than the  
31 seasonal mean for entire South Asia ( $0.47\pm 0.46$ ). Interestingly, negative UVAI was only evident during  
32 early October (week 1) signifying presence of non-absorbing aerosols (like sulphate), while the  
33 dominance of UV absorbing aerosols such as smoke and/or mineral dust was evident during rest of



1 the season. During BDP, the high UVAI values ( $>1.5$ ) were mainly found to concentrate over the upper  
2 to middle IGP with 72 % of observations remain  $>1.0$ . This clearly indicates the larger abundance of  
3 fresh UV-absorbing particles, and is similar to the reported UVAI ( $<2.0$ ) over the Himalayas during peak  
4 burning season (Kumar et al., 2011; Vadrevu et al., 2012). There was also considerable difference  
5 between the periodical mean UVAI for BDP ( $1.47\pm 0.64$ ) and BLDP ( $0.75\pm 0.58$ ) over the ground station.  
6 Further, following Guan et al. (2010) to use UVAI as a proxy to compute aerosol height, we found a  
7 low average height of aerosol layer ( $\sim 1.5$  km), possibly due to low-altitude injection of plumes from  
8 burning of agricultural residues.

9        Apart from aerosols, spatial variation of few trace gases (e.g. CO and NO<sub>2</sub>), directly emitted  
10 from biomass burning are also estimated. The MERRA-2 reanalysis surface CO profile was consistent  
11 with the observed UVAI, with high CO surface concentration over IGP (mean $\pm$ SD:  $156\pm 62$  ppbv) in  
12 comparison to South Asia ( $114\pm 52$  ppbv). Similar was the case for tropospheric NO<sub>2</sub> column density as  
13 Aura OMI observations show consistent variation across IGP ( $2.4\pm 1.1 \times 10^{15}$  mol.cm<sup>-2</sup>) with reference  
14 to South Asia ( $1.5\pm 1.0 \times 10^{15}$  mol.cm<sup>-2</sup>). There was definite spatial signature of the influence of biomass  
15 emissions on these trace gases, while their abundance may also have influenced by other  
16 anthropogenic sources (like industry and vehicular emissions). Likewise, higher surface NO<sub>2</sub>  
17 concentrations ( $> 5 \times 10^{15}$  mol cm<sup>-2</sup>) were particularly evident over Punjab and Delhi, over industrial  
18 sectors in the Chhattisgarh and in lower IGP (particularly over Dhaka). Episode specific spatial  
19 variations in mean CO (143 to 169 ppbv) and NO<sub>2</sub> concentrations ( $2.3$  to  $2.5 \times 10^{15}$  mol cm<sup>-2</sup>) were not  
20 so radical both across IGP and over the ground station (CO: 140-142 ppbv; NO<sub>2</sub>:  $2.3$ - $2.5 \times 10^{15}$  mol cm<sup>-2</sup>).  
21 The possible explanation for such minimum episode-specific variation may be the short residence  
22 time of NO<sub>2</sub> and CO, as NO<sub>2</sub> rapidly photo-dissociate by reaction with OH radical, while CO gradually  
23 oxidized to form CO<sub>2</sub>. Overall, spatio-temporal nature of aerosol and trace gases were consistent with  
24 the observed trend at the ground station and were prudent for establishing the influence of biomass  
25 emissions over the region.

### 26 **3.7 Vertical distribution of aerosols**

27        Vertically resolved aerosol subtypes from spaceborne lidar for selected overpasses across IGP  
28 are plotted in Fig. 8a, with corresponding extinction coefficient of aerosol type (Fig. 8b). The CALIPSO-  
29 CALIOP profile clearly indicates a temporal change in aerosol type, without any considerable change  
30 in the height of aerosol layer. During initial days (in October), dominance of polluted dust (dust mixed  
31 with biomass burning smoke) were noted across IGP, with occasional prevalence of smoke (biomass  
32 burning aerosols), clean continental (clean background aerosol) and dust aerosols. However, the  
33 contribution of polluted dust to total aerosol extinction was higher compared to the rest of aerosol  
34 type. The height of aerosol layer was relatively low ( $<1.5$  km) corresponding to a low plume injection





1 height and thereby, pose limited potential for dispersion. The aerosol vertical profile however,  
2 modified from the end of October due to biomass burning emissions, with dominance of smoke  
3 particles, mainly persisting at low altitude (<1.5 km). The height of smoke layer was consistent to that  
4 of OMI UVAI projected aerosol height. Smoke particles were found to associate with polluted dust,  
5 clean continental and polluted continental, with overlapping profiles. Overall, smoke was the most  
6 frequent aerosol type with high aerosol extinction coefficient ( $1\text{--}2.5\text{ km}^{-1}$  at 532 nm), and the altitude  
7 of largest occurrence frequency of smoke remain below  $\sim 1.5$  km. The low injection height of smoke  
8 plumes from biomass burning may serve as a key input for aerosol transport modeling over IGP, as it  
9 critically regulates the distance and direction of the particle dispersion (Guan et al., 2010; Banerjee et  
10 al., 2011).

11 The daily variation in total aerosol extinction and aerosol extinction only by smoke particles  
12 were also included in Fig. 8c. Total aerosol extinction indicates a corresponding increase during  
13 biomass burning which peaks particularly in November, with low smoke injection height. Clear  
14 evidence of gradual increase in smoke particle aerosol extinction was also noted. A single evidence of  
15 high smoke extinction ( $>1\text{ km}^{-1}$ ) at a greater height ( $\sim 3.4$  km) was noted on November 11, which may  
16 be associated to particles travelling from a larger distance. Overall, the CALIOP aerosol profiles were  
17 in accordance to the ground observations and OMI UVAI, referring exclusive dominance of high UV-  
18 absorbing aerosols across the plain during intense biomass burning.

### 19 **3.8 Potential aerosols sources and transport**

20 The regional transport of aerosols from western dry regions (Sen et al., 2016, 2017) and/or  
21 from middle-east Asia (Kumar et al., 2015, 2017b, 2018) through prevailing westerlies are often  
22 considered as a prominent contributor of aerosols across IGP. There are also reports of gradual  
23 accumulation of fine particles at lower altitude from north-western dry regions (Kumar et al., 2015).  
24 Considering the possibility of regional transport of biomass burning aerosols, MODIS fire counts, fire  
25 radiative power, brightness temperature along with 5-days back trajectories were included in Fig. 9.  
26 Active fire counts from the Terra and Aqua MODIS fires and thermal anomalies (with  $\geq 70\%$  confidence)  
27 clearly indicate that fire spots were predominately over the upper IGP, mainly concentrated over the  
28 Indian state of Punjab, Haryana and western Uttar Pradesh, and in Punjab state of Pakistan. However,  
29 there was a temporal shift in the total number of fire counts (Fig. 9, within the marked region) from  
30 biomass burning dominating period (BDP: 5272) to less dominating period (BLDP: 4466). Even, the Fire  
31 Radiative Power (FRP) i.e. rate of energy released in unit time indicates a relative change in amount  
32 and strength of biomass burning emissions, mainly during BDP (138,366 MW) in comparison to BLDP  
33 (112,168 MW). The total FRP was higher during BDP mainly due to higher number of fire counts and  
34 fire strength, as the rate of release of thermal radiation is related to the amount of biomass burnt and



1 smoke being released (Schroeder et al., 2010). The MODIS fire spots (with brightness temperature),  
2 specially subset over IGP were plotted against five days air-mass back trajectories, simulated and  
3 integrated at three vertical heights (100m, 300m and 500m) over the ground station. Vertical heights  
4 were selected based on the average planetary boundary layer height ( $402\pm 81$  m) for the monitoring  
5 period. The air-mass back trajectories indicate the upper IGP as the sole source of aerosols during BDP,  
6 which was otherwise influenced by both continental and marine air-masses during non-dominating  
7 period. The air-mass back trajectories during BDP overlap precisely on the fire spots that corresponds  
8 to higher brightness temperature, referring greater relevance to FRP. The air masses for individual  
9 episode were further subject to cluster and CWT analysis to quantify potential influences of aerosol  
10 source regions to total aerosol loading (Kumar et al., 2018). The CWT were drawn considering  
11 columnar aerosol load, and result was consistent with our prior observations. High CWT ( $>0.8$ ) during  
12 BDP was clearly attributed to the regional pollution, mainly originated from the upper IGP. In contrast,  
13 relatively low CWT was noted during BLDP, originating both from upper IGP ( $CWT < 0.8$ ), western dry  
14 region ( $CWT < 0.6$ ) and few from oceanic environment ( $CWT < 0.4$ ). This leads us to conclude with  
15 confidence that there was a strong temporal gradient in post-monsoon specific biomass burning  
16 emission over the upper IGP, which greatly influence the regional aerosol climatology and thereby,  
17 possibly influence the aerosol-induced health effects and regional climate.

### 18 **3.9 Aerosol radiative forcing and atmospheric heating**

19 Daily satellite retrieved AOD, TCO, CWV, SSA, ground-based BC mass concentration, aerosol  
20 water soluble and insoluble fractions were used as an input to OPAC model to simulate aerosol  
21 radiative forcing (ARF at  $0.2\text{--}4.0$   $\mu\text{m}$ ). Within the period, TCO varied between 237 to 277 DU without  
22 any difference between BDP ( $257\pm 10$  DU) and BLDP ( $256\pm 12$  DU). The SSA (at 550nm), designates the  
23 fraction of scattered light over the total light extinction, was lower during BDP ( $0.86\pm 0.05$ ) compared  
24 to BLDP ( $0.98\pm 0.04$ ), suggesting abundance of strong absorbing aerosols especially during BDP. The  
25 CWV also fluctuates considerably (range:  $0.28\text{--}3.92$  cm) with overall season specific mean ( $\pm\sigma$ ) of  $2.0$   
26 ( $\pm 0.7$ ) cm.

27 The direct ARF and heating rate were estimated under clear-sky conditions with SBDART  
28 model using OPAC output. The composite ARF was calculated for individual episodes at surface (SRF),  
29 top of the atmosphere (TOA) and atmosphere (ATM) (Fig. 10). Overall, the ARF at TOA and SRF were  
30 negative, indicating the aerosol cooling effect at surface and at top-of-the-atmosphere. There was a  
31 slight temporal change in TOA radiative forcing (BDP:  $-28$ ; BLDP:  $-23$   $\text{W m}^{-2}$ ) compared to the  
32 considerable intra-seasonal variation in SRF forcing (BDP:  $-163$ ; BLDP:  $-79$   $\text{W m}^{-2}$ ). The variation in SRF  
33 forcing was mainly induced by the surface BC (mean; BDP, BLDP:  $9$ ,  $7$   $\mu\text{g m}^{-3}$ ), aerosol mass  
34 concentration ( $501$ ,  $327$   $\mu\text{g m}^{-3}$ ) and WSIC fractions, particularly in  $\text{SO}_4^{2-}$  ( $38$ ,  $15$   $\mu\text{g m}^{-3}$ ),  $\text{NO}_3^-$  ( $19$ ,  $12$



1  $\mu\text{g m}^{-3}$ ) and  $\text{NH}_4^+$  (11, 4  $\mu\text{g m}^{-3}$ ). Since the ATM forcing is the balance of attenuation of radiation at TOA  
2 and SRF, the resultant atmospheric forcing was found very high, especially during biomass burning  
3 dominated period (BDP: 135  $\text{W m}^{-2}$ ), compared to non-dominating one (BLDP: 56  $\text{W m}^{-2}$ ). Overall, there  
4 was a clear indication of intraseasonal variation in aerosol radiative forcing, which may be useful in  
5 parametrization of aerosol schemes in regional climate model. Similarly, the corresponding heat rate  
6 was substantially high during BDP (4.3  $\text{K day}^{-1}$ ), possibly influenced by more absorbing aerosols,  
7 compared to BLDP (1.8  $\text{K day}^{-1}$ ). The computed ARF during post-monsoon was comparable to other  
8 urban sites in Indo-Gangetic Plain that are reported to be influenced by biomass burning e.g. Delhi  
9 (44-131  $\text{W m}^{-2}$ , Bisht et al., 2015), Patiala (57-63  $\text{W m}^{-2}$ , Sharma et al. 2017), Kanpur (30-43  $\text{W m}^{-2}$ ,  
10 Kaskaoutis et al., 2013) and over Karachi (35-84  $\text{W m}^{-2}$ , Alam et al., 2011). However, none of the earlier  
11 reports noted the intraseasonality in ARF by means of change in driving factors which, appeared to be  
12 significant, and necessitate proper addressing in regional model simulation. Intraseasonality in ARF  
13 was earlier reported over Varanasi during winter (ARF: 31-47  $\text{W m}^{-2}$ , Kumar et al., 2017b), while the  
14 change in forcing was not as drastic as evident during post-monsoon. Therefore, it is extremely likely  
15 that intraseasonality in aerosol properties significantly influence the aerosol-climate-health  
16 interactions over IGP and therefore, must need to be taken in to account for uncertainty analysis in  
17 the regional aerosol/-climate model.

#### 18 4. Conclusions

19 The influence of biomass burning emissions on aerosol properties, transport and radiative  
20 forcing was evaluated over Indo-Gangetic plain, South Asia. Very high concentration of total and fine  
21 mode aerosol ( $\text{PM}_{2.1}$ ) were observed during post-monsoon, with significant increase in fine to coarse  
22 particle ratio ( $>1$ ) particularly from November. Submicron particles dominate the aerosol fine mode,  
23 with  $\text{PM}_{1.1}$  to  $\text{PM}_{1.1-2.1}$  ratio frequently exceeding 2.5. The WSIS was found to constitute greater  
24 proportion of submicron and fine particle mass compared to the coarser one. The WSIS was mainly of  
25 secondary nature, with major contribution from sulfate and nitrate ions. A strong correlation between  
26  $\text{NH}_4^+$  and  $\text{SO}_4^{2-}$ , and high  $\text{NH}_4^+/\text{SO}_4^{2-}$  equivalent ratio in submicron particulates indicate the abundance  
27 of gaseous  $\text{NH}_3$  to neutralize acidic species ( $\text{SO}_4^{2-}$ ). This contrasted with coarse mode particles where  
28 low  $\text{NH}_4^+/\text{SO}_4^{2-}$  equivalent ratio refers the predominant neutralization by crustal minerals. The  $\text{NO}_3^-$  to  
29  $\text{SO}_4^{2-}$  ratio for submicron and fine mode particles also increased ( $>1$ ) during extreme biomass  
30 emissions, as expected considering other reported observations of haze events over Asia. A rise in  
31 black carbon with corresponding increase in Delta-C refer to the added contribution of biomass  
32 burning emissions. The influence of emissions was further quantified using specific molecular  
33 (Levoglucosan), inorganic ( $\text{K}^+$  and  $\text{NH}_4^+$ ) and satellite (UVAI) tracers. Levoglucosan was the most  
34 abundant species in submicron particles, with a very high ratio ( $>50$ ) against other anhydrosugars



1 denoting exclusive emissions from burning of agriculture residues. The temporal variation in  
2 levoglucosan was consistent with inorganic tracers ( $K^+$  and  $NH_4^+$ ), with a sharp rise during November,  
3 and a strong correlation between these three indicates their biogenic sources. The association  
4 between levoglucosan and  $K^+$  or  $NH_4^+$  was non-linear, with an exponential fit for submicron and fine  
5 particulates. The spatio-temporal distribution of aerosols was evaluated in terms of area weighted  
6 mean both over IGP and over the selected transect across ground station. During biomass burning  
7 dominated period, a considerable increase in columnar aerosol loading was highlighted (AOD: 0.98),  
8 consisting absorbing aerosols ( $UVAI > 1.5$ ) with a corresponding low plume height ( $\sim 1.5$  km).  
9 Moreover, the variation of few trace gases associated with biomass emissions ( $CO$  and  $NO_2$ ) were  
10 consistent with AOD, allowing a definite spatial signature of emissions sources and transport across  
11 IGP. The CALIPSO-CALIOP cross-sectional altitudinal profiles clearly illustrate the intraseasonality in  
12 aerosol types that were dominated by smoke and polluted continental aerosols during biomass  
13 emissions, which otherwise associate to clean continental, polluted dust and dust aerosols. The  
14 possible pathway for regional transport of aerosols from upper IGP to the ground station was noted  
15 using cluster analysis and concentration weighted air mass back-trajectories. Finally, aerosol optical  
16 and micro-physical properties were used in combination to simulate direct aerosol radiative forcing  
17 (ARF) and atmospheric heating. There was evidence of strong intraseasonality in ARF with very high  
18 atmospheric forcing ( $135 \text{ Wm}^{-2}$ ) and heating rate ( $4.3 \text{ Kday}^{-1}$ ) during biomass burning dominated  
19 period compared to non-dominating one ( $56 \text{ Wm}^{-2}$ ,  $1.8 \text{ Kday}^{-1}$ ).

20 Considering that the duration of these biomass burning emissions due to post-monsoon  
21 specific agricultural practices represents several weeks per year, there annual impact on ARF and by  
22 consequent on the regional climate is not negligible. We therefore, conclude with reasonable level of  
23 confidence that intraseasonality in aerosol properties must be seriously considered in the regional  
24 aerosol-climate model, for improve assessment and forecasting of aerosol-climate-health interactions  
25 across IGP.

#### 26 **Data availability**

27 MODIS data are available at Level 1 Atmosphere Archive & Distribution System (LAADS) at  
28 <https://ladsweb.nascom.nasa.gov>. Aura-OMI and MERRA 2 reanalysis data are available at Mirador-  
29 NASA Goddard Earth Sciences Data and Information Center (GES DISC)  
30 (<https://mirador.gsfc.nasa.gov>). CALIPSO data are available at NASA Atmospheric Science Data Center  
31 (<https://eosweb.larc.nasa.gov>). Planetary Boundary Layer height and air mass back-trajectories are  
32 retrieved from Global Data Assimilation System (GDAS) archives hosted at NOAA-Air Resource  
33 Laboratory (<https://ready.arl.noaa.gov>). Modis Fire products are obtained from Fire Information for  
34 Resource Management System (FIRMS) (<https://firms.modaps.eosdis.nasa.gov>). Trace gases data at



1 ground station are available at Real time Air Quality Data inventory of Central Pollution Control Board  
2 (<https://app.cpcbccr.com/ccr>).

3

4 **Team List.** Nandita Singh (NS), Tirthankar Banerjee (TB), Made P. Raju (MPR), Karine Deboudt (KD),  
5 Meytar Sorek-Hamer (MSH), Ram S. Singh (RSS) and Rajesh K. Mall (RKM).

#### 6 **Author Contributions**

7 N.S. and T.B. designed the experiment while N.S., M.P.R. and T.B. carried out the experiment and  
8 analyzed the data. N.S., M.P.R., K.D., T.B., R.S.S., R.K.M. and M.S.H. interpreted the observation and  
9 N.S., T.B. and K.D. drafted the manuscript.

10 **Competing interests.** The authors declare that they have no conflict of interest.

#### 11 **Acknowledgements**

12 The research is supported by Science and Engineering Research Board (SERB), Department of Science  
13 and Technology (DST), New Delhi (SR/FTP/ES-52/2014). T.B. acknowledges the financial support from  
14 University Grants Commission (UGC) under UGC-ISF bilateral project (6-11/2018 IC), R.S.S.  
15 acknowledges the Indian Space Research Organization (ISRO), Thiruvananthapuram under ARFI (Code:  
16 P-32-13) and R.K.M. acknowledges DST under Prime Ministers National Action Plan on Climate Change  
17 project (DST/CCP/CoE/80/2017-G). N.S. acknowledges the financial support under DST Women  
18 Scientist scheme (SR/WOS-A/EA-1012/2015) and M.S.H. acknowledges the NASA Post-Doctoral  
19 Fellowship, administered by USRA. Authors duly acknowledge the guidance and cooperation provided  
20 by Dean and Director, IESD-BHU.

#### 21 **References**

- 22 Alam, K., Trautmann, T., and Blaschke, T.: Aerosol optical properties and radiative forcing over mega-city  
23 Karachi, Atmos. Res., 101, 773-782, <https://doi.org/10.1016/j.atmosres.2011.05.007>, 2011.
- 24 Apte, J.S., Marshall, J.D., Cohen, A.J., and Brauer, M.: Addressing global mortality from ambient PM<sub>2.5</sub>, Environ.  
25 Sci. Technol., 49, 8057-8066, <https://pubs.acs.org/doi/10.1021/acs.est.5b01236>, 2015.
- 26 Badarinath, K.V.S., Sharma, A.R., Kaskaoutis, D.G., Kharol, S.K., and Kambezidis, H.D.: Solar dimming over the  
27 tropical urban region of Hyderabad, India: Effect of increased cloudiness and increased anthropogenic  
28 aerosols. J. Geophys. Res.-Atmos., 115, D21208, <https://doi.org/10.1029/2009JD013694>, 2010.
- 29 Banerjee, T., Murari, V., Kumar, M., and Raju, M.P.: Source apportionment of airborne particulates through  
30 receptor modeling: Indian scenario. Atmos. Res., 164, 167-187,  
31 <https://doi.org/10.1016/j.atmosres.2015.04.017>, 2015.
- 32 Banerjee, T., Barman, S.C., Srivastava, R.K.: Application of air pollution dispersion modeling for source-  
33 contribution assessment and model performance evaluation at Integrated Industrial Estate-Pantnagar.  
34 Environ Pol., 159, 865-875, <https://doi.org/10.1016/j.envpol.2010.12.026>, 2011.
- 35 Bellouin, N., Boucher, O., Haywood, J., and Reddy, M.S.: Global estimate of aerosol direct radiative forcing from  
36 satellite measurements, Nature, 438, 1138-1141, <https://doi.org/10.1038/nature04348>, 2005.



- 1 Bisht, D.S., Dumka, U.C., Kaskaoutis, D.G., Pipal, A.S., Srivastava, A.K., Soni, V.K., Attri, S.D., Sateesh, M., and  
2 Tiwari, S.: Carbonaceous aerosols and pollutants over Delhi urban environment: temporal evolution,  
3 source apportionment and radiative forcing, *Sci. Total Environ.*, 521, 431-445,  
4 <https://doi.org/10.1016/j.scitotenv.2015.03.083>, 2015.
- 5 Bodhaine, B.A.: Aerosol absorption measurements at Barrow, Mauna Loa and the south pole, *J. Geophys. Res.-*  
6 *Atmos.*, 100, 8967-8975, <https://doi.org/10.1029/95JD00513>, 1995.
- 7 Bond, T.C., Doherty, S.J., Fahey, D.W., Forster, P.M., Berntsen, T., DeAngelo, B.J., Flanner, M.G., Ghan, S.,  
8 Kärcher, B., Koch, D., and Kinne, S.: Bounding the role of black carbon in the climate system: A scientific  
9 assessment, *J. Geophys. Res.-Atmos.*, 118, 5380-5552, <https://doi.org/10.1002/jgrd.50171>, 2013.
- 10 Chang-Graham, A.L., Profeta, L.T., Johnson, T.J., Yokelson, R.J., Laskin, A. and Laskin, J.: Case study of water-  
11 soluble metal containing organic constituents of biomass burning aerosol, *Environ. Sci. Technol.*, 45,1257-  
12 1263, <https://doi.org/10.1021/es103010j>, 2011.
- 13 Cheng, Y., Engling, G., He, K.B., Duan, F.K., Ma, Y.L., Du, Z.Y., Liu, J.M., Zheng, M., and Weber, R.J.: Biomass  
14 burning contribution to Beijing aerosol, *Atmos. Chem. Phys.*, 13(15), 7765-7781,  
15 <https://doi.org/10.5194/acp-13-7765-2013>, 2013.
- 16 Draxler, R.R., and Rolph, G.D., 2003. HYSPLIT (HYbrid single-particle Lagrangian integrated trajectory) model  
17 access via NOAA ARL READY. NOAA Air Resources Laboratory, Silver Spring, MD. Dostupno na:  
18 <http://ready.arl.noaa.gov/HYSPLIT.php> (06. 06. 2010.).
- 19 Engling, G., Lee, J.J., Tsai, Y.W., Lung, S.C.C., Chou, C.C.K., and Chan, C.Y.: Size-resolved anhydrosugar  
20 composition in smoke aerosol from controlled field burning of rice straw, *Aerosol Sci. Technol.*, 43, 662-  
21 672, <https://doi.org/10.1080/02786820902825113>, 2009.
- 22 Fu, P., Kawamura, K., Okuzawa, K., Aggarwal, S.G., Wang, G., Kanaya, Y., and Wang, Z.: Organic molecular  
23 compositions and temporal variations of summertime mountain aerosols over Mt. Tai, North China  
24 Plain, *J. Geophys. Res.-Atmos.*, 113, D19107, <https://doi.org/10.1029/2008JD009900>, 2008.
- 25 Gonzalez, R.O., Strekopytov, S., Amato, F., Querol, X., Reche, C., and Weiss, D.: New insights from zinc and copper  
26 isotopic compositions into the sources of atmospheric particulate matter from two major European  
27 cities, *Environ. Sci. Technol.*, 50, 9816-9824, <https://pubs.acs.org/doi/10.1021/acs.est.6b00863>, 2016.
- 28 Guan, H., Esswein, R., Lopez, J., Bergstrom, R., Warnock, A., Follette-Cook, M., Fromm, M., and Iraci, L.T.: A multi-  
29 decadal history of biomass burning plume heights identified using aerosol index measurements, *Atmos.*  
30 *Chem. Phys.*, 10, 6461-6469, <https://doi.org/10.5194/acp-10-6461-2010>, 2010.
- 31 Hess, M., Koepke, P., and Schult, I.: Optical properties of aerosols and clouds: The software package OPAC, *Bull.*  
32 *Am. Meteorol. Soc.*, 79, 831-844, [https://doi.org/10.1175/1520-0477\(1998\)079<0831:OPOAAC>2.0.CO;2](https://doi.org/10.1175/1520-0477(1998)079<0831:OPOAAC>2.0.CO;2), 1998.
- 34 Hu, Q.H., Xie, Z.Q., Wang, X.M., Kang, H., and Zhang, P.: Levoglucosan indicates high levels of biomass burning  
35 aerosols over oceans from the Arctic to Antarctic, *Sci. Rep.*, 3, 3119, <https://doi.org/10.1038/srep03119>,  
36 2013.
- 37 Jimenez, J.L., Canagaratna, M.R., Donahue, N.M., Prevot, A.S.H., Zhang, Q., Kroll, J.H., DeCarlo, P.F., Allan, J.D.,  
38 Coe, H., Ng, N.L., and Aiken, A.C.: Evolution of organic aerosols in the atmosphere, *Science*, 326, 1525-  
39 1529, <http://doi.org/10.1126/science.1180353>, 2009.
- 40 Justice, C., Giglio, L., Boschetti, L., Roy, D., Csiszar, I., Morissette, J., and Kaufman, Y.: MODIS Fire Products  
41 Algorithm Technical Background Document. MODIS Science Team, 2006.
- 42 Kanakidou, M., Myriokefalitakis, S., and Tsigaridis, K.: Aerosols in atmospheric chemistry and biogeochemical  
43 cycles of nutrients. *Environ. Res. Lett.*, in press, <https://doi.org/10.1088/1748-9326/aabccb>, 2018.



- 1 Kaskaoutis, D.G., Kumar, S., Sharma, D., Singh, R.P., Kharol, S.K., Sharma, M., Singh, A.K., Singh, S., Singh, A., and  
2 Singh, D.: Effects of crop residue burning on aerosol properties, plume characteristics, and long-range  
3 transport over northern India, *J. Geophys. Res.-Atmos.*, **119**, 5424-5444,  
4 <https://doi.org/10.1002/2013JD021357>, 2014.
- 5 Kaskaoutis, D.G., Sinha, P.R., Vinoj, V., Kosmopoulos, P.G., Tripathi, S.N., Misra, A., Sharma, M., and Singh, R.P.:  
6 Aerosol properties and radiative forcing over Kanpur during severe aerosol loading conditions, *Atmos.*  
7 *Environ.*, **79**, 7-19, <https://doi.org/10.1016/j.atmosenv.2013.06.020>, 2013.
- 8 Krotkov, N.A., Lamsal, L.N., Celarier, E.A., Swartz, W.H., Marchenko, S.V., Bucsela, E.J., Chan, K.L., Wenig, M., and  
9 Zara, M.: The version 3 OMI NO<sub>2</sub> standard product, *Atmospheric Meas. Tech.*, **10**, 3133-3149,  
10 <https://doi.org/10.5194/amt-10-3133-2017>, 2017.
- 11 Kumar, M., Parmar, K.S., Kumar, D.B., Mhawish, A., Broday, D.M., Mall, R.K., and Banerjee, T.: Long-term aerosol  
12 climatology over Indo-Gangetic Plain: Trend, prediction and potential source fields, *Atmos. Environ.*, **180**,  
13 37-50, <https://doi.org/10.1016/j.atmosenv.2018.02.027>, 2018.
- 14 Kumar, M., Raju, M.P., Singh, R.S., and Banerjee, T.: Impact of drought and normal monsoon scenarios on aerosol  
15 induced radiative forcing and atmospheric heating in Varanasi over middle Indo-Gangetic Plain, *J. Aerosol*  
16 *Sci.*, **113**, 95-107, <https://doi.org/10.1016/j.jaerosci.2017.07.016>, 2017a.
- 17 Kumar, M., Raju, M.P., Singh, R.K., Singh, A.K., Singh, R.S., and Banerjee, T.: Wintertime characteristics of aerosols  
18 over middle Indo-Gangetic Plain: Vertical profile, transport and radiative forcing, *Atmos. Res.*, **183**, 268-  
19 282, <https://doi.org/10.1016/j.atmosres.2016.09.012>, 2017b.
- 20 Kumar, M., Singh, R.K., Murari, V., Singh, A.K., Singh, R.S., and Banerjee, T.: Fireworks induced particle pollution:  
21 a spatio-temporal analysis, *Atmos. Res.*, **180**, 78-91, <https://doi.org/10.1016/j.atmosres.2016.05.014>,  
22 2016.
- 23 Kumar, M., Tiwari, S., Murari, V., Singh, A.K., and Banerjee, T.: Wintertime characteristics of aerosols at middle  
24 Indo-Gangetic Plain: Impacts of regional meteorology and long range transport, *Atmos. Environ.*, **104**,  
25 162-175, <https://doi.org/10.1016/j.atmosenv.2015.01.014>, 2015.
- 26 Kumar, R., Naja, M., Satheesh, S.K., Ojha, N., Joshi, H., Sarangi, T., Pant, P., Dumka, U.C., Hegde, P., and  
27 Venkataramani, S.: Influences of the springtime northern Indian biomass burning over the central  
28 Himalayas, *J. Geophys. Res.-Atmos.*, **116**, D19302, <https://doi.org/10.1029/2010JD015509>, 2011.
- 29 Kang, M., Fu, P., Aggarwal, S.G., Kumar, S., Zhao, Y., Sun, Y., and Wang, Z.: Size distributions of n-alkanes, fatty  
30 acids and fatty alcohols in springtime aerosols from New Delhi, India, *Environ. Pollut.*, **219**, 957-  
31 966, <https://doi.org/10.1016/j.envpol.2016.09.077>, 2016.
- 32 Levelt, P.F., van den Oord, G.H., Dobber, M.R., Malkki, A., Visser, H., de Vries, J., Stammes, P., Lundell, J.O., and  
33 Saari, H.: The ozone monitoring instrument, *IEEE Trans. Geosci. Remote Sens.*, **44**, 1093-1101,  
34 <http://doi.org/10.1109/TGRS.2006.872333>, 2006.
- 35 Levy, R.C., Mattoo, S., Munchak, L.A., Remer, L.A., Sayer, A.M., Patadia, F., and Hsu, N.C.: The Collection 6 MODIS  
36 aerosol products over land and ocean, *Atmospheric Meas. Tech.*, **6**, 2989-3034,  
37 <https://doi.org/10.5194/amt-6-2989-2013>, 2013.
- 38 Li, J., Wang, G., Aggarwal, S.G., Huang, Y., Ren, Y., Zhou, B., Singh, K., Gupta, P.K., Cao, J., and Zhang, R.:  
39 Comparison of abundances, compositions and sources of elements, inorganic ions and organic  
40 compounds in atmospheric aerosols from Xi'an and New Delhi, two megacities in China and India, *Sci.*  
41 *Total Environ.*, **476**, 485-495, <https://doi.org/10.1016/j.scitotenv.2014.01.011>, 2014.
- 42 Mochida, M., Umemoto, N., Kawamura, K., Lim, H.J., and Turpin, B.J.: Bimodal size distributions of various  
43 organic acids and fatty acids in the marine atmosphere: Influence of anthropogenic aerosols, Asian dusts,  
44 and sea spray off the coast of East Asia, *J. Geophys. Res.-Atmos.*, **112**,  
45 D15209, <https://doi.org/10.1029/2006JD007773>, 2007.



- 1 Mhawish, A., Banerjee, T., Broday, D.M., Misra, A., and Tripathi, S.N.: Evaluation of MODIS Collection 6 aerosol  
2 retrieval algorithms over Indo-Gangetic Plain: Implications of aerosols types and mass loading, *Remote*  
3 *Sens. Environ.*, 201, 297-313, <https://doi.org/10.1016/j.rse.2017.09.016>, 2017.
- 4 Mhawish, A., Kumar, M., Mishra, A.K., Srivastava, P.K., and Banerjee, T.: Remote sensing of aerosols from space:  
5 retrieval of properties and applications, In *Remote Sensing of Aerosols, Clouds, and Precipitation*, 45-83,  
6 <https://doi.org/10.1016/B978-0-12-810437-8.00003-7>, 2018.
- 7 Moorthy, K.K., Satheesh, S.K., Babu, S.S., and Dutt, C.B.S.: Integrated Campaign for Aerosols, gases and Radiation  
8 Budget (ICARB): An overview, *J. Earth Syst. Sci.*, 117, 243–262, [https://doi.org/10.1007/s12040-008-](https://doi.org/10.1007/s12040-008-0029-7)  
9 0029-7, 2008.
- 10 Murari, V., Kumar, M., Barman, S.C., and Banerjee, T.: Temporal variability of MODIS aerosol optical depth and  
11 chemical characterization of airborne particulates in Varanasi, India, *Environ. Sci. Pollut. Res.*, 22, 1329-  
12 1343, <https://doi.org/10.1007/s11356-014-3418-2>, 2015.
- 13 Murari, V., Kumar, M., Mhawish, A., Barman, S.C., and Banerjee, T.: Airborne particulate in Varanasi over middle  
14 Indo-Gangetic Plain: variation in particulate types and meteorological influences, *Environ. Monit.*  
15 *Assess.*, 189, 157, <https://doi.org/10.1007/s10661-017-5859-9>, 2017.
- 16 Murari, V., Kumar, M., Singh, N., Singh, R.S., and Banerjee, T.: Particulate morphology and elemental  
17 characteristics: variability at middle Indo-Gangetic Plain, *J. Atmos. Chem.*, 73, 165-179,  
18 <https://doi.org/10.1007/s10874-015-9321-5>, 2016.
- 19 Myhre, G., Samset, B.H., Schulz, M., Balkanski, Y., Bauer, S., Berntsen, T.K., Bian, H., Bellouin, N., Chin, M., Diehl,  
20 T., and Easter, R.C.: Radiative forcing of the direct aerosol effect from AeroCom Phase II  
21 simulations, *Atmos. Chem. Phys.*, 13, 1853-1877, <https://doi.org/10.5194/acp-13-1853-2013>, 2013.
- 22 Pavuluri, C.M., Kawamura, K., Aggarwal, S.G., and Swaminathan, T.: Characteristics, seasonality and sources of  
23 carbonaceous and ionic components in the tropical aerosols from Indian region, *Atmos. Chem. Phys.*, 11,  
24 8215-8230, <https://doi.org/10.5194/acp-11-8215-2011>, 2011.
- 25 Prajapati, S.K., and Tripathi, B.D.: Seasonal variation of leaf dust accumulation and pigment content in plant  
26 species exposed to urban particulates pollution, *J. Environ. Qual.*, 37, 865-870,  
27 <https://doi.org/10.2134/jeq2006.0511>, 2008.
- 28 Rajput, P., and Sarin, M.M.: Polar and non-polar organic aerosols from large-scale agricultural-waste burning  
29 emissions in Northern India: implications to organic mass-to-organic carbon ratio, *Chemosphere*, 103, 74-  
30 79, <https://doi.org/10.1016/j.chemosphere.2013.11.028>, 2014.
- 31 Rajput, P., Sarin, M. M., Sharma, D., and Singh, D.: Characteristics and emission budget of carbonaceous species  
32 from post-harvest agricultural-waste burning in source region of the Indo-Gangetic Plain, *Tellus B*, 66,  
33 21026, <https://doi.org/10.3402/tellusb.v66.21026>, 2014
- 34 Rajput, P., Sarin, M.M., Rengarajan, R., and Singh, D.: Atmospheric polycyclic aromatic hydrocarbons (PAHs) from  
35 post-harvest biomass burning emissions in the Indo-Gangetic Plain: isomer ratios and temporal  
36 trends, *Atmos. Environ.*, 45, 6732-6740, <https://doi.org/10.1016/j.atmosenv.2011.08.018>, 2011.
- 37 Raju, M.P., Safai, P.D., Vijayakumar, K., Devara, P.C.S., Naidu, C.V., Rao, P.S.P., and Pandithurai, G.: Atmospheric  
38 abundances of black carbon aerosols and their radiative impact over an urban and a rural site in SW  
39 India, *Atmos. Environ.*, 125, 429-436, <https://doi.org/10.1016/j.atmosenv.2015.09.023>, 2016.
- 40 Ricchiazzi, P., Yang, S., Gautier, C., and Sowle, D.: SBDART: A research and teaching software tool for plane-  
41 parallel radiative transfer in the Earth's atmosphere, *Bull. Am. Meteorol. Soc.*, 79, 2101-2114,  
42 [https://doi.org/10.1175/1520-0477\(1998\)079<2101:SARATS>2.0.CO;2](https://doi.org/10.1175/1520-0477(1998)079<2101:SARATS>2.0.CO;2), 1998.
- 43 Riipinen, I., Pierce, J.R., Yli-Juuti, T., Nieminen, T., Hakkinen, S., Ehn, M., Junninen, H., Lehtipalo, K., Petaja, T.,  
44 Slowik, J., and Chang, R.: Organic condensation: a vital link connecting aerosol formation to cloud





- 1 condensation nuclei (CCN) concentrations, Atmos. Chem. Phys., 11, 3865-3878,  
2 <https://doi.org/10.5194/acp-11-3865-2011>, 2011.
- 3 Rogers, R.R., Hostetler, C.A., Hair, J.W., Ferrare, R.A., Liu, Z., Obland, M.D., Harper, D.B., Cook, A.L., Powell, K.A.,  
4 Vaughan, M.A., and Winker, D.M.: Assessment of the CALIPSO Lidar 532 nm attenuated backscatter  
5 calibration using the NASA LaRC airborne High Spectral Resolution Lidar, Atmos. Chem. Phys., 11, 1295-  
6 1311, <https://doi.org/10.5194/acp-11-1295-2011>, 2011.
- 7 Ryu, S.Y., Kim, J.E., Zhuanshi, H., Kim, Y.J. and Kang, G.U.: Chemical composition of post-harvest biomass burning  
8 aerosols in Gwangju, Korea, J. Air Waste Manag. Assoc., 54, 1124-  
9 1137, <https://doi.org/10.1080/10473289.2004.10471018>, 2004.
- 10 Sayer, A.M., Munchak, L.A., Hsu, N.C., Levy, R.C., Bettenhausen, C., and Jeong, M.J.: MODIS Collection 6 aerosol  
11 products: Comparison between Aqua's e-Deep Blue, Dark Target, and "merged" data sets, and usage  
12 recommendations, J. Geophys. Res.-Atmos., 119, 13,965–13,989,  
13 <https://doi.org/10.1002/2014JD022453>, 2014.
- 14 Schkolnik, G., Falkovich, A.H., Rudich, Y., Maenhaut, W., and Artaxo, P.: New analytical method for the  
15 determination of levoglucosan, polyhydroxy compounds, and 2-methylerythritol and its application to  
16 smoke and rainwater samples, Environ. Sci. Technol., 39, 2744-2752, <http://doi.org/10.1021/es048363c>,  
17 2005.
- 18 Schroeder, W., Csiszar, I., Giglio, L., and Schmidt, C.C.: On the use of fire radiative power, area, and temperature  
19 estimates to characterize biomass burning via moderate to coarse spatial resolution remote sensing data  
20 in the Brazilian Amazon, J. Geophys. Res.-Atmos., 115, D21121, <https://doi.org/10.1029/2009JD013769>,  
21 2010.
- 22 Seinfeld, J.H., Bretherton, C., Carslaw, K.S., Coe, H., DeMott, P.J., Dunlea, E.J., Feingold, G., Ghan, S., Guenther,  
23 A.B., Kahn, R., and Kraucunas, I.: Improving our fundamental understanding of the role of aerosol– cloud  
24 interactions in the climate system, Proc. Natl. Acad. Sci., 113, 5781-5790,  
25 <https://doi.org/10.1073/pnas.1514043113>, 2016.
- 26 Sen, A., Abdelmaksoud, A.S., Ahammed, Y.N., Banerjee, T., Bhat, M.A., Chatterjee, A., Choudhuri, A.K., Das, T.,  
27 Dhir, A., Dhyani, P.P., and Gadi, R.: Variations in particulate matter over Indo-Gangetic Plains and Indo-  
28 Himalayan Range during four field campaigns in winter monsoon and summer monsoon: role of pollution  
29 pathways, Atmos. Environ., 154, 200-224, <https://doi.org/10.1016/j.atmosenv.2016.12.054>, 2017.
- 30 Sen, A., Ahammed, Y.N., Banerjee, T., Chatterjee, A., Choudhuri, A.K., Das, T., Deb, N.C., Dhir, A., Goel, S., Khan,  
31 A.H., and Mandal, T.K.: Spatial variability in ambient atmospheric fine and coarse mode aerosols over  
32 Indo-Gangetic plains, India and adjoining oceans during the onset of summer monsoons, 2014, Atmos.  
33 Pollut. Res., 7, 521-532, <https://doi.org/10.1016/j.apr.2016.01.001>, 2016.
- 34 Sharma, D., Srivastava, A.K., Ram, K., Singh, A., and Singh, D.: Temporal variability in aerosol characteristics and  
35 its radiative properties over Patiala, northwestern part of India: Impact of agricultural biomass burning  
36 emissions, Environ. Pollut., 231, 1030-1041, <https://doi.org/10.1016/j.envpol.2017.08.052>, 2017.
- 37 Simoneit, B.R., Schauer, J.J., Nolte, C.G., Oros, D.R., Elias, V.O., Fraser, M.P., Rogge, W.F., and Cass, G.R.:  
38 Levoglucosan, a tracer for cellulose in biomass burning and atmospheric particles, Atmos. Environ., 33,  
39 173-182, [https://doi.org/10.1016/S1352-2310\(98\)00145-9](https://doi.org/10.1016/S1352-2310(98)00145-9), 1999.
- 40 Singh, N., Murari, V., Kumar, M., Barman, S.C., and Banerjee, T.: Fine particulates over South Asia: review and  
41 meta-analysis of PM<sub>2.5</sub> source apportionment through receptor model, Environ. Pollut., 223, 121-136,  
42 <https://doi.org/10.1016/j.envpol.2016.12.071>, 2017a.
- 43 Singh, N., Mhawish, A., Deboudt, K., Singh, R.S., and Banerjee, T.: Organic aerosols over Indo-Gangetic Plain:  
44 Sources, distributions and climatic implications, Atmos. Environ., 157, 59-74,  
45 <https://doi.org/10.1016/j.atmosenv.2017.03.008>, 2017b.



- 1 Sun, J., and Ariya, P.A.: Atmospheric organic and bio-aerosols as cloud condensation nuclei (CCN): A review,  
2 Atmos. Environ. 40, 795–820, <https://doi.org/10.1016/j.atmosenv.2005.05.052>, 2006.
- 3 Tan, J.H., Duan, J.C., Chen, D.H., Wang, X.H., Guo, S.J., Bi, X.H., Sheng, G.Y., He, K.B., and Fu, J.M.: Chemical  
4 characteristics of haze during summer and winter in Guangzhou, Atmos. Res., 94, 238–245,  
5 <https://doi.org/10.1016/j.atmosres.2009.05.016>, 2009.
- 6 Tian, M., Wang, H., Chen, Y., Yang, F., Zhang, X., Zou, Q., Zhang, R., Ma, Y., and He, K.: Characteristics of aerosol  
7 pollution during heavy haze events in Suzhou, China. Atmos. Chem. Phys., 16, 7357–7371,  
8 <https://doi.org/10.5194/acp-16-7357-2016>, 2016.
- 9 Torres, O., Ahn, C., and Chen, Z.: Improvements to the OMI near-UV aerosol algorithm using A-train CALIOP and  
10 AIRS observations, Atmospheric Meas. Tech., 6, 3257–3270, <https://doi.org/10.5194/amt-6-3257-2013>,  
11 2013.
- 12 Vadrevu, K.P., Ellicott, E., Giglio, L., Badarinath, K.V.S., Vermote, E., Justice, C., and Lau, W.K.: Vegetation fires in  
13 the himalayan region—Aerosol load, black carbon emissions and smoke plume heights, Atmos.  
14 Environ., 47, 241–251, <https://doi.org/10.1016/j.atmosenv.2011.11.009>, 2012.
- 15 Vakkari, V., Kerminen, V.M., Beukes, J.P., Tiitta, P., Zyl, P.G., Josipovic, M., Venter, A.D., Jaars, K., Worsnop, D.R.,  
16 Kulmala, M., and Laakso, L.: Rapid changes in biomass burning aerosols by atmospheric  
17 oxidation, Geophys. Res. Lett., 41, 2644–2651, <https://doi.org/10.1002/2014GL059396>, 2014.
- 18 Wan, X., Kang, S., Li, Q., Rupakheti, D., Zhang, Q., Guo, J., Chen, P., Tripathee, L., Rupakheti, M., Panday, A.K.,  
19 and Wang, W.: Organic molecular tracers in the atmospheric aerosols from Lumbini, Nepal, in the  
20 northern Indo-Gangetic Plain: influence of biomass burning, Atmos. Chem. Phys., 17, 8867–8885,  
21 <https://doi.org/10.5194/acp-17-8867-2017>, 2017.
- 22 Wang, Y., Hopke, P.K., Rattigan, O.V., Xia, X., Chalupa, D.C., and Utell, M.J.: Characterization of residential wood  
23 combustion particles using the two-wavelength aethalometer, Environ. Sci. Technol., 45, 7387–7393,  
24 <http://doi.org/10.1021/es2013984>, 2011.
- 25 Wang, Y.Q., Zhang, X.Y., and Arimoto, R.: The contribution from distant dust sources to the atmospheric  
26 particulate matter loadings at XiAn, China during spring, Sci. Total Environ., 368, 875–883,  
27 <https://doi.org/10.1016/j.scitotenv.2006.03.040>, 2006.
- 28 Wang, R., Balkanski, Y., Boucher, O., Bopp, L., Chappell, A., Ciais, P., Hauglustaine, D., Peñuelas, J. and Tao, S.:  
29 Sources, transport and deposition of iron in the global atmosphere, Atmos. Chem. Phys., 15, 6247–  
30 6270, <https://doi.org/10.5194/acp-15-6247-2015>, 2015.
- 31 Zdrahal, Z., Oliveira, J., Vermeylen, R., Claeys, M., and Maenhaut, W.: Improved method for quantifying  
32 levoglucosan and related monosaccharide anhydrides in atmospheric aerosols and application to samples  
33 from urban and tropical locations, Environ. Sci. Technol., 36, 747–753,  
34 <http://doi.org/10.1021/es015619v>, 2002.
- 35 Zhang, W., Tong, Y., Wang, H., Chen, L., Ou, L., Wang, X., Liu, G. and Zhu, Y.: Emission of metals from pelletized  
36 and uncompressed biomass fuels combustion in rural household stoves in China, Sci. Rep., 4,  
37 5611, <https://doi.org/10.1038/srep05611>, 2014.
- 38



1 **List of figures:**

---

2 Fig. 1. Geographical location of aerosol ground monitoring station (a), and MODIS aerosol optical  
3 depth with NCEP/NCAR composite means of wind vector during monitoring period (b).

4 Fig. 2. Time series of (a) size segregated particulate mass concentration, (b) particle ratio and (c) daily  
5 means of meteorological variables.

6 Fig. 3. Variation of (a) ions and (b) trace metals in different aerosol size fractions.

7 Fig. 4. Variation of BC, Delta C and ABL during entire monitoring period.

8 Fig. 5. Size-segregated particulate bound (a) organic aerosols, and difference in the molecular  
9 compositions of (b) *n*-alkanes and (b) fatty acids.

10 Fig. 6. Temporal variation of trace gases and biomass burning signature molecules ( $\text{NH}_4^+$ ,  $\text{K}^+$ ,  
11 Levoglucosan), and their associations within different aerosol size fractions.

12 Fig. 7. Episode specific spatial distribution of AOD, AE, UVAI, surface CO (ppbv) and tropospheric  $\text{NO}_2$   
13 ( $\text{molecules cm}^{-2}$ ) over (a) South Asia and (b) at ground station.

14 Fig. 8. Aerosol vertical profiles from selected CALIPSO overpasses across ground station (a) aerosol  
15 subtypes, (b) extinction coefficients of each aerosol type and (c) time series of extinction profile  
16 for total and smoke aerosols.

17 Fig. 9. Episode specific MODIS fire count, fire radiative power (FRP, MW), brightness temperature (B.  
18 Temp., K), and five days air mass back-trajectory along with CWT.

19 Fig. 10. Episode specific aerosol short wave radiative forcing and atmospheric heating.

20

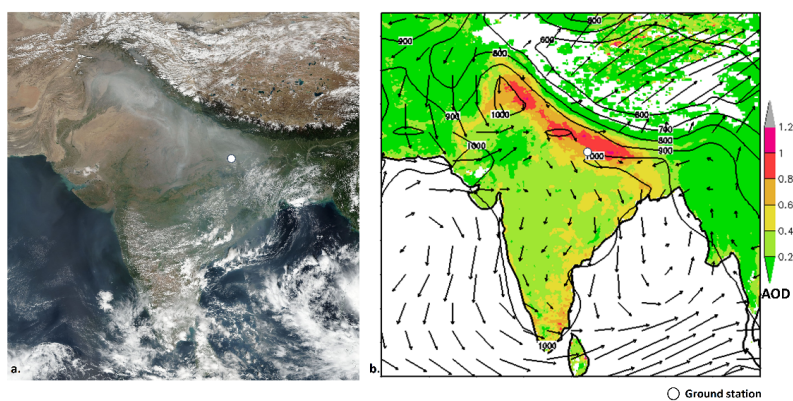
21

22

23



1  
2  
3



4  
5

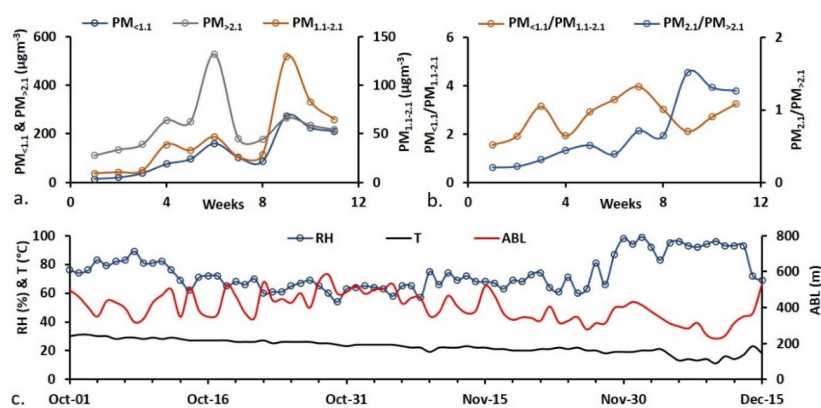
6 Fig. 1. Geographical location of aerosol ground monitoring station (a), and MODIS aerosol optical  
7 depth with NCEP/NCAR composite means of wind vector during monitoring period (b).

8 **Note:** Background image in (a) was retrieved from Suomi NPP VIIRS satellite indicating the thick  
9 aerosol layer over north India on October 31, 2016.

10



1



2

3 Fig. 2. Time series of (a) size segregated particulate mass concentration, (b) particle ratio and (c) daily  
4 means of meteorological variables.

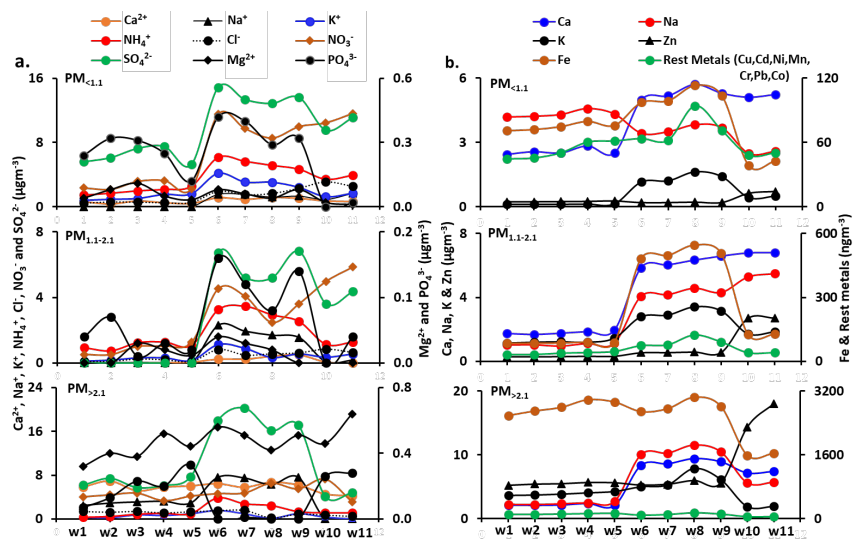
5 **Note:** Week 1 to 5 are in the month of October, week 6 to 9 are in November and week 10 to 11 are  
6 in December.

7

8



1



2

3

4

Fig. 3. Variation of (a) ions and (b) trace metals in different aerosol size fractions.

5

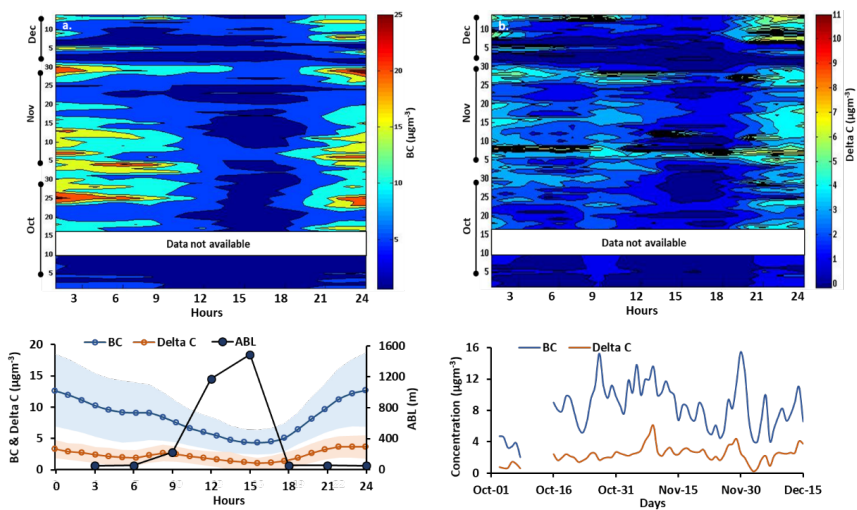
**Note:** Week 1 to 5 are in the month of October, week 6 to 9 are in November and week 10 to 11 are in December.

6

7



1  
2



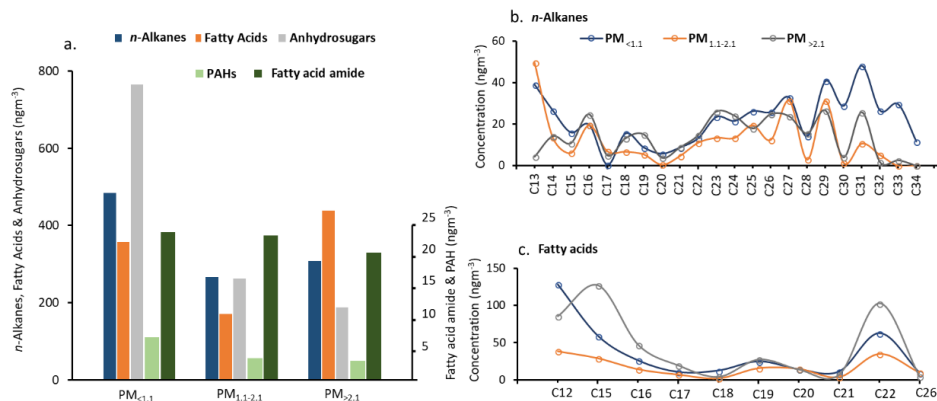
3  
4  
5  
6  
7  
8

Fig. 4. Variation of BC, Delta C and ABL during entire monitoring period.

**Note.** The blue and red shade in the graph at lower panel indicates the standard deviation.



1



2

3

4

5

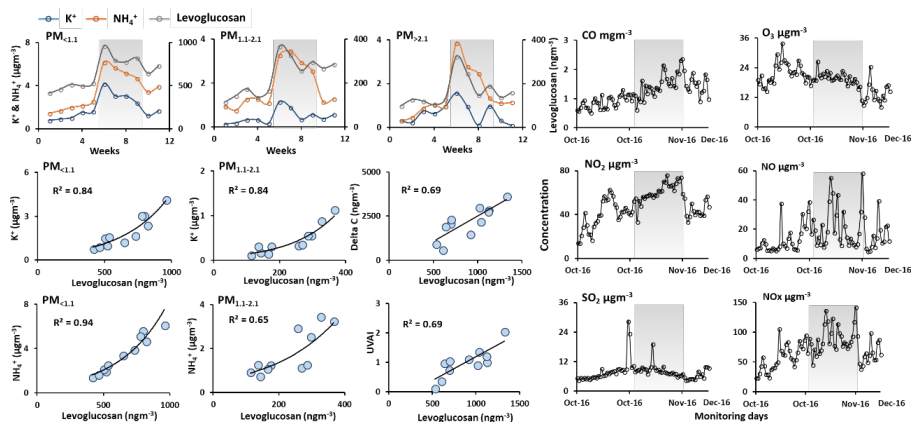
6

Fig. 5. Size-segregated particulate bound (a) organic aerosols, and difference in the molecular compositions of (b) *n*-alkanes and (c) fatty acids.





1



2

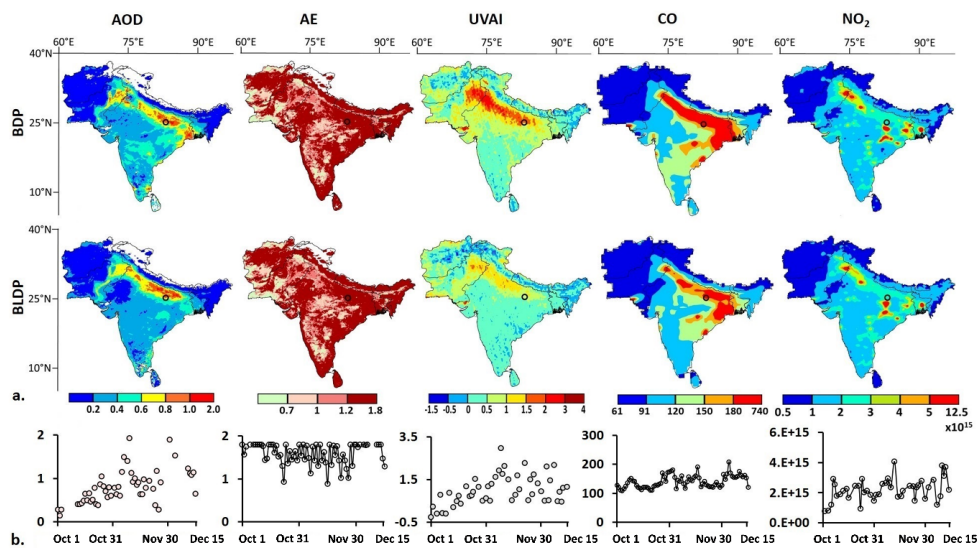
3

4 Fig. 6. Temporal variation of trace gases and biomass burning signature molecules ( $\text{NH}_4^+$ ,  $\text{K}^+$ ,  
5 Levoglucosan), and their associations within different aerosol size fractions.

6 **Note.** The shaded area indicates the peak biomass burning emissions.



1



2

3

4

5

Fig. 7. Episode specific spatial distribution of AOD, AE, UVAI, surface CO (ppbv) and tropospheric NO<sub>2</sub> (molecules cm<sup>-2</sup>) over (a) South Asia and (b) at ground station.

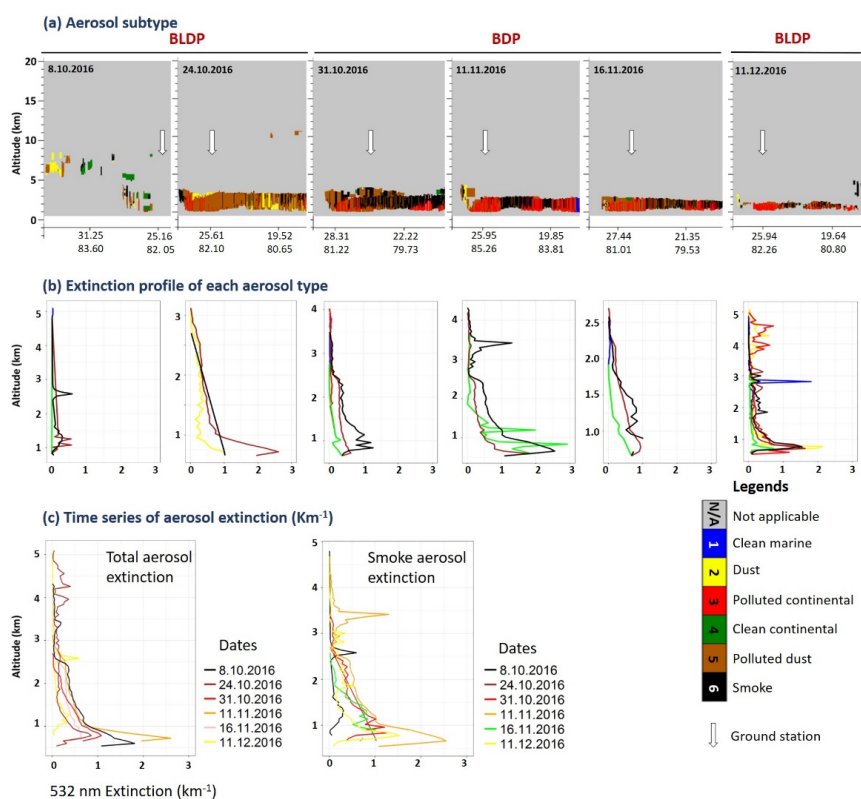
6

**Note.** The lower panel indicates the time-series for each parameter retrieved particularly over the ground station.

8



1



2

3

4

Fig. 8. Aerosol vertical profiles from selected CALIPSO overpasses across ground station (a) aerosol subtypes, (b) extinction coefficients of each aerosol type and (c) time series of extinction profile for total and smoke aerosols.

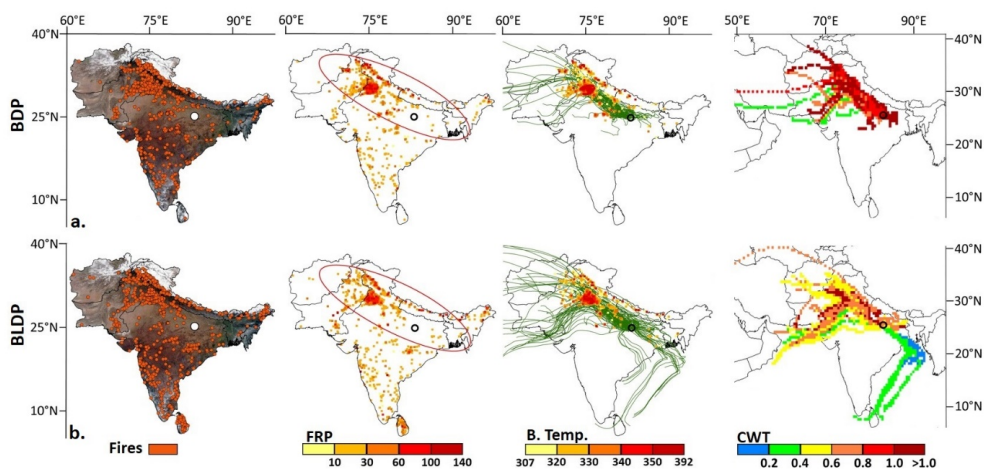
5

6

7



1



2

3

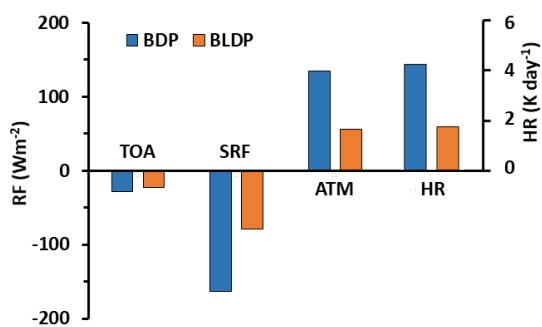
4 Fig. 9. Episode specific MODIS fire count, fire radiative power (FRP, MW), brightness temperature (B.  
5 Temp., K), and five days air mass back-trajectory along with CWT.

6

7



1



2

3

4

Fig. 10. Episode specific aerosol short wave radiative forcing and atmospheric heating.

5

6